

Fabrication of versatile nanocomposite materials for advanced energy storage systems

Emmanuel Siaw, MSc Chemical and Materials Engineering

**Submitted in fulfillment of the requirements for the Master of Science degree in
Chemical and Materials Engineering**



School of Engineering and Digital Science

Department of Chemical and Materials Engineering,

Nazarbayev University

53 Kabanbay Batyr Avenue, Astana, Kazakhstan, 010000

Lead Supervisor: Professor Stavros Pouloupoulos

Co-supervisor: Dr. Nurzhan Baikalov

Date: May 13, 2026

DECLARATION

I hereby declare that this manuscript, entitled “Fabrication of versatile nanocomposite materials for advanced energy storage systems”, is the result of my own work except for quotations and citations, which have been duly acknowledged.

I also declare that, to the best of my knowledge and belief, it has not been previously or concurrently submitted, in whole or in part, for any other degree or diploma at Nazarbayev University or any other national or international institution.



Name: Emmanuel Siaw
Date: 13th May 2026

Acknowledgment

Firstly, It would be a great pleasure for me to express my gratitude to my principal supervisor, Professor Stavros Pouloupoulos, and co-supervisor, Dr Nurzhan Baikalov, for all the help they have rendered in carrying out this research. From day-to-day meetings to weekly supervision sessions, from mentorship to advice, and from providing materials and guidelines for carrying out this work successfully. Even with their tight daily schedules, they have always had time to guide me on what I ought to do. Moreover, they have always provided me with positive comments, which have enabled me to achieve the set goals.

In addition, I wish to make use of this golden chance to express gratitude to two of my fellow group members, Mr Diaz Bekeshov and Mr Alas Alaskhanov, and the whole Battery Group, for all their contributions through knowledge exchange, which have been instrumental towards achieving what I have been able to achieve so far. You guys have been superb.

I want to express my sincere gratitude to Nazarbayev University and the Government of the Republic of Kazakhstan for their generous support through the Abai Kunanbayev Scholarship. I am also grateful to the Science Committee of the Ministry of Science and Higher Education of the Republic of Kazakhstan for funding this research under grant No AP23490764, without which this thesis would not have been possible. Moreover, I want to express my sincere gratitude to Nazarbayev University and its administration for the privilege of conducting research in such an exceptional place, which possesses all the best qualities, including well-equipped research labs and cultural diversity. This achievement has really opened doors in my quest for academic excellence.

Lastly, I want to extend my deepest appreciation to my wonderful parents, brothers, and sisters, who have been with me all along, offering their moral, emotional, and mental support. I am deeply grateful for all the support.

Abstract

In general, the energy density capacity of the Li-S battery is exceptional, reaching a value of 2600 Wh kg^{-1} , nearly five times higher than that of the lithium-ion battery. However, the application of this technology faces a lot of challenges because of the polysulfides shuttle effect and redox reaction that results in the kinetic capacity loss of the electrode material. In this current study, anatase phase TiO_2 nanotubes with a size of approximately 18.3 nm were fabricated by the hydrothermal technique as a multifunctional additive in three different forms: TiO_2 nanotubes, nickel oxide decorated TiO_2 nanotubes (NiO/TiO_2), and nickel metal-modified TiO_2 nanotubes (Ni/TiO_2). These materials were deposited onto carbon fibre paper to fabricate cathode materials. It should be noted that TiO_2 has a high polarity nature and acts as a good adsorbent for polysulfides, but the material is characterized by poor electron conductivity and catalytic activity. After decoration with NiO nanoparticles, TiO_2 can demonstrate improved ability for chemisorption and oxidation-reduction of polysulfides. Nickel metal nanoparticles decoration improves electronic conductivity and facilitates interfacial reaction. According to all analyzed cells, the one that contains Ni/TiO_2 electrode provides a superior energy output with a specific capacity of 1285 mAh g^{-1} and after 100 cycles, obtained 1095 mAh g^{-1} at the sulfur load of 4 mg cm^{-2} under 0.2 C discharge rate. It was observed that the same cell maintains distinguished charge-discharge plateaus without polarization after 100 cycles. The minimum transfer resistance of 14Ω and maximum Li_2S nucleation of 746 mAh g^{-1} have been achieved by using Ni/TiO_2 .

Table of Contents

Declaration	2
Acknowledgements	3
Abstract	4
List of Figures	7
List of Tables	9
List of Abbreviations	8
1 Chapter One – Introduction	12
1.1 Problem Statement	14
1.2 Scope of Study	15
1.3 Objectives of the Study	15
1.4 Study Significance	15
2 Chapter Two – Literature Review	17
2.1 Polysulfide Shuttle Effect and Kinetic Challenges in Lithium- Sulfur Batteries	17
2.1.1 Polysulfide Shuttle Effect: Mechanism and Impact.....	17
2.1.2 Strategies for shuttle suppression.....	17
2.1.3 Kinetic Challenges associated with Lithium Sulfur Batteries	17
2.1.4 Advances in Kinetic Enhancement	18
2.2 Metal oxide nanostructures (1D, 2D, 3D, nanospheres, nanoparticles, nanotubes) and applications. .	18
2.2.1 General applications of metal oxide nanostructures	18
2.2.2 Uses of metal oxide nanostructures in lithium sulfur batteries.	19
2.3 Types and Forms of Titanium Dioxide (TiO ₂)	20
2.3.1 Titanium Dioxide (TiO ₂).....	20
2.3.2 Phases of Titanium Dioxide TiO ₂	20
2.4 TiO ₂ Nanotubes: Synthesis Routes, Phase Control, Defect Introduction, and Properties.	20
2.5 Synthesis Methods	20
2.5.1 Phase Engineering.....	21
2.6 Nickel-Based Materials: Nickel Oxide (NiO), Metallic Ni Systems.....	21
2.6.1 Nickel Oxide	21

2.6.2	Metallic Ni (Nickel Nanoparticles	22
2.7	Integration Strategies and Synergistic Effects for Decorated Systems	22
2.8	Challenges and Future Directions: Optimization, Scalability, and Interfacial Engineering of TiO ₂ Nanotubes Decorated with NiO/Ni.....	22
3	Chapter Three – Methodology	24
3.1	Preparation of TiO ₂ Nanotubes decorated with Nickel oxide/Nickel nanoparticles	24
3.2	Preparation of Cathode Materials	25
3.3	Cell Assembly	25
3.4	Materials characterization.....	26
3.5	Electrochemical Characterization	26
3.6	Symmetric cell test.....	26
3.7	Nucleation test	27
4	RESULTS AND DISCUSSION.....	28
4.1	Physical Characterization of TiO ₂ nanotube-based samples	28
4.2	Effect on the kinetics of redox	32
4.3	Cycling performance of modified TiO ₂ -based cathodes.....	37
5	Conclusion	41
	References.....	42

List Of Figures

- Fig. 1** Schematic illustration depicting the synthesis route of (a) TiO₂ nanotubes and (b) Decoration of NiO and Ni nanoparticles on the nanotubes.25
- Fig. 2** Physical characterization of TiO₂, NiO/TiO₂, Ni/TiO₂ nanotubes: (a) XRD pattern, (b) TGA, (c) nitrogen adsorption-desorption isotherms, (d) pore size distribution and (e) ICP OES.29
- Fig. 3** SEM images of nanotubes(a) TiO₂, (b) NiO/TiO₂, (c) Ni/TiO₂; low-resolution TEM image of Ni/TiO₂ nanotubes at (d) 50 nm, (e) 100 nm and (f) HRTEM images of Ni/TiO₂ (d-spacing).30
- Fig. 4** SEM image of Ni/TiO₂-CFP electrodes at (a) 0.5 μm, (b) 1 μm, (c) 100 nm; EDS mappings of Ni/TiO₂ electrodes at (d) 100 nm.31
- Fig. 5** XPS characterization of TiO₂-CF, NiO/TiO₂-CFP, and Ni/TiO₂-CFP electrodes after soaking in Li₂S₆ solution (a) Ti 2p, (b) O 1s and (c) Ni 2p (1) and Ni 2p (2).32
- Fig. 6** Comparative cyclic voltammetry (CV) curves at 0.1 mV s⁻¹ for all electrodes: (a) TiO₂-CFP, (b) NiO/TiO₂-CFP and (c) Ni/TiO₂-CFP.33
- Fig. 7** CV profiles of electrodes recorded at various scan rates ranging from 0.1 to 0.5 mV s⁻¹:(a) TiO₂-CFP, (b) NiO/TiO₂-CFP and (c) Ni/TiO₂-CFP, (d-f) The linear fittings of the peak currents versus the square root of the scan rates (v^{1/2}).34
- Fig. 8** CV curves of Li₂S₆ symmetric cells with NiO/TiO₂ and Ni/TiO₂ based electrodes at varying scan rates: (a) 1 mV s⁻¹, (b) 10 mV s⁻¹ and (c) 20 mV s⁻¹.35
- Fig. 9** Potentiostatic discharge of cells with (a) TiO₂-CFP, (b) NiO/TiO₂-CFP and (c) Ni/TiO₂-CFP.36
- Fig. 10** Electrochemical Impedance Spectroscopy profiles for cells with TiO₂-based electrodes.36
- Fig. 11** (a-b) Charge-discharge cycling performance of cells with TiO₂-CFP, NiO/TiO₂-CFP and Ni/TiO₂-CFP cathodes at 0.5 C and 1 C, respectively, (c) rate capability test of TiO₂-CFP,

NiO/TiO₂-CFP and Ni/TiO₂-CFP cathodes, respectively and (d) Charge-discharge cycling performance of the cell.38

Fig. 12 (a) galvanostatic charge-discharge profiles of cells with TiO₂-CFP, NiO/TiO₂-CFP and Ni/TiO₂-CFP cathodes at the 5th cycle and (b) galvanostatic charge-discharge profiles of cells with Ni/TiO₂-CFP cathodes at the 2nd, 5th, 10th, 50th and 100th cycle, respectively.39

List Of Tables

Table 1. Li^+ diffusion coefficient ($D(\text{Li}^+)$) values of TiO_2 , NiO/TiO_2 and Ni/TiO_2	35
Table 2. Comparison of the electrochemical performance of TiO_2 -based nanotubes.....	24

List of Abbreviations and Symbols

TiO ₂	Titanium dioxide
NiO	Nickel (II) Oxide
Ni	Metallic Nickel
Li ₂ S	Lithium sulfide
Li ₂ S ₆	Lithium HexaSulfide
S ₈	Elemental Sulfur
NaOH	Sodium Hydroxide
HCl	Hydrochloric Acid
SEM	Scanning Electron Microscopy
TEM	Transmission Electron Microscopy
XRD	X-ray Diffraction
TGA	Thermogravimetric Analysis
XPS	X-ray Photoelectron Spectroscopy
EDS	Energy Dispersive X-ray Spectroscopy
ICP-OES	Inductively Coupled Plasma Optical Emission Spectroscopy
CV	Cyclic Voltammetry
EIS	Electrochemical Impedance Spectroscopy
BET	Brunauer-Emmett-Teller
BJH	Barrett-Joyner-Halenda
LiPSs	Lithium polysulfide species
Li-S	Lithium-Sulfur battery
LIBs	Lithium-ion batteries
CFP	Carbon fiber paper
PVDF	Polyvinylidene fluoride
NMP	N-methyl-2-pyrrolidone
	1,3-dioxolane and 1,2- dimethoxyethane (electrolyte solvents)
DOL/DME	

LiTFSI

Lithium

bis(trifluoromethanesulfonyl)imide

LiNO₃

Lithium nitrate

R_{ct}

Charge transfer resistance

1 Chapter One – Introduction

The rapid growth of the renewable energy sector and the onset of electric vehicle technology have set off a chain reaction in the pursuit of improved energy storage solutions. We seek energy storage solutions that offer higher energy density values, longer cycle life, and greater safety. Current lithium-ion batteries (LIBs) have achieved their peak in general application capabilities in terms of their theoretical limit for a given capacity and energy density[1-3]. The need for alternative battery technologies has therefore become a prominent trend in materials science.

Lithium sulfur batteries (Li-S batteries) have been identified as one of the promising alternatives for the next generation of storage batteries because of the high theoretical specific capacity (approximately 1675 mAhg^{-1}) and energy density of about 2600 Wh/kg , significantly higher than that of conventional LIBs [3]. Sulfur, the active component of the cathode in Li-S batteries, is abundant in nature, very cheap, and eco-friendly. This further adds to the attraction of this technology [1]. These merits make Li-S batteries a promising candidate for applications ranging from storage to the highly competitive domains of portable electronics and electric vehicles. Despite the theoretical merits of Li-S batteries, there have been many challenges in the practical implementation of the technology.

The realization of Li-S batteries faces several challenges in terms of material characteristics. For example, sulfur and the product of a chemical reaction that takes place during the processes of a battery, lithium sulfide (Li_2S), have very low electrical conductivity [3-5]. This low conductivity makes the use of conductive additives necessary in the cathode. These additives may add to the weight of the cathode[3, 4]. A second significant problem is known as the “polysulfide shuttle effect.” In the redox reaction process of Li-ion batteries, intermediate lithium polysulfides (Li_2S_x , $4 \leq x \leq 8$) dissolve in the electrolyte between the electrodes [1, 3]. This results in the loss of active material, self-discharge, and fast capacity depletion, together with low coulombic efficiency. These factors also include the dissolution or migration of polysulfides in the creation of electrically insulating layers on the lithium anode surface[3-5]. Additionally, the high volumetric expansion of sulfur (80%) that takes place in the lithiation process creates a high degree of stress in the cathode material. The growth of lithium dendrites in the battery cycle also poses a serious safety risk of a short circuit or thermal

runaway. All in all, the problems mentioned above have been identified to affect the cycle life, efficiency of energy conversion, and application of Li-S batteries[3, 5].

To overcome these challenges, there has been significant research on the development of highly advanced cathode material designs. Graphene, CNTs, and porous carbon have been extensively used as sulfur hosts to improve conductivity properties to effectively confine polysulfides[1, 6]. These offer high surface area values and a conductive network to promote sulfur utilization and rates of reaction[7, 8]. Metal oxides (such as TiO₂, MnO₂, NiO) and metal-organic frameworks (MOFs) have also been proposed as polar hosts or interlayers to chemically adsorb polysulfides [9]. Conductive polymers, including polypyrrole and polyaniline, have also been investigated for their capability of sulfur encapsulation and flexibility enhancement of electrodes[10]. The hybrid nanostructures comprising combinations of carbon material with metal oxides/conductive polymers have shown evidence of synergism, providing advantages in terms of polysulfide retention capability, catalysis, and strength [9].

Within the context of these strategies, TiO₂ nanocomposites have received immense attention for their unique combination of chemical stability, high polysulfide adsorption capacity, and flexibility in forming nanostructures [11-14]. Based on these strategies, one promising candidate for the advancement of Li-S batteries would be the application of anatase TiO₂ nanotubes. The one-dimensional nature of these nanotubes enables a high surface area for the accommodation of active polysulfides [13].

Anatase TiO₂ nanotubes demonstrate some unique merits for the application of the cathode additive in Li-S batteries. The one-dimensional nanoscale structure of the TiO₂ nanotubes enables a higher surface area that provides more sites for the adsorption of polysulfides [15-19]. Additionally, the tubular structure enables the material to cope well with the volume change process in the lithiation and delithiation cycles [16, 17].

Moreover, NiO nanoparticles decoration of the TiO₂ nanotubes brings in new functionalities. NiO is a transition metal oxide exhibiting high Lewis acidity. It has the capability to form strong chemical bonds with polysulfide ions, further lowering their dissolution & migration [20, 21]. Furthermore, NiO also possesses catalytic functionality in terms of increasing the redox reaction between polysulfides. This further improves the overall kinetics of the reaction in the cathode. The combination of TiO₂ and NiO provides a strong synergistic effect in terms of confining the polysulfides both physically and chemically [22], [23]. The addition of metallic Ni nanoparticles tackles the problem of low electronic

conductivity in both sulfur and metal oxides. Ni nanoparticles act as high-conductivity channels to ensure efficient electron transfer in the cathode composition[20]. Additionally, the coexistence of Ni and NiO may also form more catalytic interfaces, thereby facilitating the reversible absorption and desorption of polysulfides. In summary, the ternary TiO₂-NiO/Ni nanocomposite possesses the merits of strong adsorption capability of polysulfides, high catalytic activity, and high electrical conductivity. This provides a holistic solution to the complex issues in Li-S batteries [21].

Although titanium dioxide has received significant attention due to its polar characteristics, it has not found extensive use in batteries due to its low electronic conductivity and limited kinetic performance. In this study, three anatase phase TiO₂ nanotube-based additives with an average nanotube diameter of approximately 18.3 nm were synthesized via hydrothermal synthesis, which led to the formation of TiO₂ nanotubes. The TiO₂ nanotubes were then modified with NiO and Ni nanoparticles. These materials were specifically designed to have double functionality of lithium polysulfide immobilization and promotion of conversion reactions at the same time under the condition of high sulfur mass content. They were tested as active cathode components in the form of composite electrodes, incorporated into carbon fibre paper substrates. Though the cathode TiO₂ has shown decent capacity to absorb lithium polysulfides, its efficiency was hampered by low conductivity and low activity towards catalysis. However, the electrode with NiO/TiO₂ has improved ability for chemical adsorption and redox reaction, while Ni/TiO₂ improved conductivity and reaction rates.

1.1 Problem Statement

The scaling-up of lithium sulfur batteries is challenged by issues of polysulfide shuttling, low redox reaction rates, low electrical conductivity, and sulfur loading. While TiO₂ nanotube-containing lithium sulfur batteries benefit from polar adsorption sites, their low electrical conductivity is a drawback. The use of TiO₂ nanotubes decorated with Ni/NiO can improve adsorption, conversion, and electrical conductivity. However, questions remain on how much, where, and in what form of Ni/NiO and TiO₂ should be used. There are also no scalable preparation methods, and very limited work describes Li-S battery performance above 400 Wh/kg operation with sulfur loading above 2 mg/cm². There, hence, appears a challenge in developing a rationally designed, scalable Ni/NiO@TiO₂ composite host that can be used to facilitate Li-S batteries with high energy and long-term stability.

1.2 Scope of Study

This research aims to synthesize, optimize, and investigate Ni/NiO decorated anatase TiO₂ nanotube-based multifunctional host materials for lithium sulfur batteries. This research encompasses the development of the composite structure using both hydrothermal and thermal processing, as well as a thorough analysis of morphology, structure, and surface properties using common analytical techniques. This research also aims to investigate the electrochemical properties, stability, and resistance to polysulfide leakage for practical sulfur loadings above 2 mg/cm². Prototype cell tests are also performed to check the validity of achieving energy densities above 400 Wh/kg. This research, however, does not cover the development of optimized electrolytes, separators, and integration with battery packs, as it will primarily focus on host-sulfur interactions related to the composition and structure of battery components.

1.3 Objectives of the Study

The primary aim of this research work is to design and optimize Ni/NiO-modified TiO₂ nanotube composites for improved performance of Li-S batteries. The research aims to optimize the loading, distribution, and phase composition of Ni/NiO on TiO₂ nanotube structures and identify structure-property correlations. It also aims to develop high-performance Li-S batteries that can function with sulfur loading over 2 mg/cm². Furthermore, this research work aims to develop scalable processes for the mass production of nanocomposite materials, as well as design a lithium sulfur battery prototype that can provide energy densities over 400 Wh/kg.

1.4 Study Significance

On a scientific basis, this work promotes a deeper comprehension of the role of Ni/NiO composition and distribution over TiO₂ nanotubes in relation to polysulfide adsorption and catalytic conversion, in addition to offering fundamental insights for efficient design strategies for sulfur host materials with versatile properties. On a technological basis, it contributes to further advancements in high-loading Li-S batteries with a stable Li-S cathode meeting commercial performance benchmarks in a composite host that combines adsorption capabilities, catalytic properties, and electrical conductivity.

1.5 Structure of the Thesis

This thesis is organized into five chapters. Chapter One presents the introduction, which covers the background of lithium-sulfur batteries, the problem statement, scope of study, objectives, and significance of the study. Chapter Two provides a review of the relevant literature on Li-S

battery challenges, cathode host materials, and the role of TiO_2 and Ni/NiO-based nanocomposites in improving battery performance. Chapter Three describes the materials, synthesis methods, and characterization techniques used in this study, including hydrothermal synthesis and the various analytical tools employed. Chapter Four presents and discusses the experimental results, covering the structural, morphological, and electrochemical performance of the synthesized TiO_2 , NiO/ TiO_2 , and Ni/ TiO_2 composites. Chapter Five concludes the thesis by summarizing the key findings, drawing conclusions, and offering recommendations for future research.

2 Chapter Two – Literature Review

2.1 Polysulfide Shuttle Effect and Kinetic Challenges in Lithium-Sulfur Batteries

2.1.1 Polysulfide Shuttle Effect: Mechanism and Impact

The Polysulfide Shuttle Effect occurs because the lithium polysulfides formed react to dissolve in and diffuse into the electrolyte solution due to their chemical nature during the cycle of the battery cells. The dissolved species move from the positive electrode to the negative electrode, where parasitic chemical reactions occur involving lithium metal [24, 25]. The shuttle process involves a series of steps: the formation of long-chain polysulfides, their release from the sulfur host, dissolution in the electrolyte solution, transport to the anode side, and the subsequent chemical reaction with lithium [26]. The extent to which the shuttle effect occurs depends upon the polysulfide species solubility, size, and mobility, and the key species to affect the shuttle effect has been discovered to be Li_2S_4 based on its favorable solubility and mobility characteristics [27-29].

2.1.2 Strategies for shuttle suppression

Below is a list of strategies for shuttle suppression.

- i. Physical confinement of sulfur and or polysulfides in cathode host matrices and interlayers [24, 30].
- ii. Chemical adsorption based on the high affinity of certain materials towards LiPSs, for instance, Mn_3O_4 and functionalized separators [31, 32].
- iii. Catalytic conversion to enhance the rate of polysulfide redox reactions and minimize their presence in solutions [33].
- iv. Electrolyte engineering to restrict the solubility of polysulfides or facilitate their selective transport [34, 35].

2.1.3 Kinetic Challenges Associated with Lithium Sulfur Batteries

The redox reactions in these batteries, and the deposition of lithium sulfide (Li_2S), naturally involve low kinetics. The low kinetics are reflected in high polarization, low sulfur utilization efficiency, and limited rate capability [29, 36]. For the lean electrolyte/solvent conditions, activation polarization, associated with the low interfacial transfer rate, is found to

be a major hindrance to kinetics [35]. The kinetics are also hindered by the Li_2S crystallization process, while methods for the enhanced deposition of amorphous Li_2S have shown promise in facilitating redox reactions [36].

2.1.4 Advances in Kinetic Enhancement

Current research focuses on, firstly, catalyst design, in the form of metal oxides, selenides, and two-site catalysts, to lower the energy activation and facilitate both the solid-electrolyte interphase reaction (SRR) and the sulfur evolution reaction (SER)[37, 38]. Secondly, he designed separators and cathode structures to work in a synergistic manner to improve lithium-ion and polysulfide utilization [39]. Thirdly, redox mediators/electrolyte additives to improve fast electron and ion transport [34, 35].

2.2 Metal oxide nanostructures (1D, 2D, 3D, nanospheres, nanoparticles, nanotubes) and applications.

Metal oxides, such as TiO_2 , ZnO , and their counterparts, exhibit a wide range of morphologies: 1D, 2D, and 3D architecture, nanospherical, nanoparticulate, and nanotubular structures, and each has proven to offer unique properties in terms of applications in energy storage, catalysis, and sensing.

2.2.1 General applications of metal oxide nanostructures

2.2.1.1 One-dimension (1D) nanostructures (nanotubes, nanowire and nanorods)

The properties of the resultant 1D metal oxides include large surface area, anisotropic conduction of ions and electrons, and improved mechanical stability. The applications of the properties include gas sensors, EC devices, LEDs, supercapacitor electrodes, and nanoelectronics because the properties can be tailor-made through proper control of their morphology [40, 41].

2.2.1.2 Two-dimensional (2D) nanostructures (nanosheets and nanoplates)

The large surface area to volume and availability of active sites make two-dimensional metal oxides promising materials in the applications of optoelectronics, sensors, and electrochemical energy storage. The two-dimensional structure of metal oxides allows them to exhibit properties that are not present in their three-dimensional counterparts due to their extremely thin dimensions [42-44].

2.2.1.3 Three-dimension (3D) Nanostructures (Hierarchical, Porous and Branched)

The resulting 3D architecture, designed through the combination of 1D and/or 2D components, offers a conduit structure for efficient ion/electron transport and high surface area properties applicable to batteries, supercapacitor electrodes, and catalysts [42, 45].

2.2.1.4 Nanospheres and Nanoparticles

Metal oxide nanospheres and nanoparticles find applications in catalysis, gas sensors, energy applications, and biomedical fields because of their size controllability, high reactivity, and surface chemistry properties [45].

2.2.2 Uses of metal oxide nanostructures in lithium sulfur batteries.

2.2.2.1 Polysulfide Adsorption and Shuttle Suppression

Nanostructured metal oxides, such as TiO_2 , NiCoO_2 , and MgO , are excellent hosts/conduction interlayers. The materials chemistry strongly absorbs lithium polysulfides, thus preventing the shuttle effect [47, 48].

2.2.2.2 Improving Conductivity and Catalysis

Hybrid architectures, for example, metal oxide/C nanotube composites, overcome the issue of low electrical conductivity in metal oxides and offer active sites for the conversion of polysulfides, thereby ensuring faster rates and stable cycling [48].

2.2.2.3 Morphology-dependent performance

Below is a list of nanostructures with respect to performance.

- i. 1D Nanostructures (nanotubes, nanowires): Assist in fast electron/ion transport and polysulfide confinement [41, 49].
- ii. 2D Nanostructures: Employed in the separator domain or coating layers to inhibit the diffusion of polysulfides, while ensuring the transport of ions [42, 43].
- iii. 3D architecture: Provide interlaced networks for high sulfur capacity, fast electron/ion transfer, and high adsorption density [48].
- iv. Nanospheres and nanoparticles: These morphologies both encase sulfur and enhance the chemical adsorption to improve sulfur utilization and inhibit volume expansion [50].

2.3 Types and Forms of Titanium Dioxide (TiO₂)

2.3.1 Titanium Dioxide (TiO₂)

Titanium dioxide (TiO₂) is a popular and well-studied material, known for its stability, availability, and applications. The properties and performance of TiO₂ are characterized by the presence of its crystalline phases (forms), size, and shape of the particles.

2.3.2 Phases of Titanium Dioxide TiO₂

Below is a list of different phases of titanium dioxide.

i. Anatase: Tetragonal, band gap ~ 3.2 eV: Highly reactive and is usually the most preferred form used in many applications. More stable at the nanoscale and can be transformed to rutile at relatively higher temperatures ($\sim 700^\circ\text{C}$)[51-53].

ii. Rutile: Tetragonal, band gap ~ 3.0 eV: Most stable phase in terms of thermodynamics in the bulk state. Most commonly employed in the form of a white pigment and in photocatalysis, but less active than the anatase phase in photocatalysis processes [51-53].

iii. Brookite: Orthorhombic band gap ~ 3.4 eV: Less common and less stable than anatase and rutile, but in some instances having the same or even higher photocatalytic activity [51].

iv. TiO₂ (B) and Other Forms: TiO₂ (B) is a metastable phase of monoclinic structure and has been investigated mostly concerning batteries and photocatalysis [52]. Other TiO₂ forms include the Amorphous TiO₂ and the Magnéli phases of TiO_{2n-1}[54].

2.4 TiO₂ Nanotubes: Synthesis Routes, Phase Control, Defect

Introduction, and Properties.

TiO₂ Nanotubes (TNTs) have attracted many researchers because of their unique structures and possible applications in the fields of photocatalysis and energy conversion. Structure and applications of TiO₂ Nanotubes depend on the methods for preparing TNTs and its phases.

2.5 Synthesis Methods

Firstly, the hydrothermal process involves treating TiO₂ precursors in basic solutions at higher temperatures, followed by an acid wash and annealing process. The nanotube structure, dimensions, and quality of the tubes and the crystals formed are controlled through the process. The process requires an acid wash to remove Na⁺ ions to attain pure nanotubes, and the

annealing temperature, crucial in forming the nanotube structure, is carried out at temperatures in the range of 400-600 degrees Celsius; temperatures higher than 600 degrees Celsius lead to decomposition of the nanotubes and anatase-to-rutile transformation.[55-57].

The anodization of titanium foil in the presence of fluoride electrolytes leads to the growth of well-ordered, vertically aligned TNTs. The process allows control of the diameter, height, and thickness of the tubes in accordance with the applied voltage and electrolyte concentration. The anodized TNTs outperform the hydrothermal tubes in terms of orderliness, hydrophilicity, and photoelectrochemical properties[58-60]. Other methods that can be employed to produce TNTs include template-assisted methods and the sol-gel process, but their occurrences are less frequent [61].

2.5.1 Phase Engineering

Phase engineering encompasses the regulation of the crystalline phase of TNTs, namely anatase, rutile, brookite, and the amorphous phase, because the phase has a great effect on the electronics and the catalytic properties:

- i. Anatase phase is preferable in the applications of photocatalysis and energy storage because of its large surface area and suitable band structure [58]
- ii. Biphasic/hybrid phases (e.g., anatase/rutile, and amorphous/anatase) are possible and represent a means to improve the performance [11, 55].
- iii. Atmospheric control (air, N₂, H₂) in the annealing process offers an additional capability to adjust the phase composition and density of defects [62].

2.6 Nickel-Based Materials: Nickel Oxide (NiO), Metallic Ni Systems

Nickel-based materials have varying structures and properties. These make them useful for use in the fields of catalysis, energy storage, sensing, and environmental applications. This is a highlight of the synthesis, structure, and properties of NiO, metallic Ni, and hybrid systems of Ni and NiO.

2.6.1 Nickel Oxide

Nickel Oxide (NiO) is known to be an extrinsic semiconductor with a cubic structure. NiO nanomaterials can be prepared using several different techniques, among which sol-gel, hydrothermal, green, and microfluidic processes are a few. Through these processes, the size, shapes (nanoparticles, nanosheets, nanowires), and crystalline nature[63].

Also, nickel oxide nanoparticles have a high surface area, chemical stability, and good electrochemical and photocatalytic properties. They have been used in batteries, supercapacitors, sensors, and antimicrobial applications. Morphology and the method of preparation of NiO nanoparticles greatly influence their properties, and nanosheets with a porous structure are found to have better electrochemical properties [64].

2.6.2 Metallic Ni (Nickel Nanoparticles)

Ni metallic nanoparticles are usually produced by reduction processes (for example, by γ -radiation, chemical reduction), and the sizes vary from several nanometers to several hundred nanometers. Surface oxidation can result in the formation of thin layers of Ni [65]. Also, it is ferromagnetic, highly conducting, and a good catalyst. It is used as a catalyst, magnetic material, or as the active component of energy storage devices. Surface passivation using Ni can potentially improve the reversibility of the electrochemical processes [66].

2.7 Integration Strategies and Synergistic Effects for Decorated Systems

Decorated systems, where one material is integrated or 'decorated' with another, are very important for the enhancement of the functionality of materials. The manner of material integration, or strategies, is very important for the pursuit of new functionality.

2.8 Challenges and Future Directions: Optimization, Scalability, and Interfacial Engineering of TiO₂ Nanotubes Decorated with NiO/Ni

TiO₂ nanotubes (TNTs) functionalized with a NiO/Ni catalyst possess immense potential as a catalyst in photocatalysis, electrocatalysis, and energy systems. There are, however, numerous issues hampering their practical application. To reach optimal performance, it needs precise adjustment of NiO/Ni compositions, particle size, as well as their distribution on TNTs. Overloading of NiO could cause particle aggregation, hence decreasing catalytic surface area and charge separation efficiency [67]. Secondly, NiO nanoparticles can increase the TiO₂ bandgap, which enhances the absorption of visible light and reduces recombination rates. The ratio of NiO to TiO₂ needs to be optimized. Finally, Stability and Reusability: High stability and reusability of catalysts from different cycles are critical. There are a few studies that show relatively good stability, but long-term stability in rough conditions has been a point of concern [68].

Anatase TiO₂ nanotubes modified with NiO and Ni nanoparticles represent a promising multifunctional additive material for Li-S battery cathodes, capable of addressing several

critical challenges simultaneously, including low electrical conductivity, the polysulfide shuttle effect, and poor cycling stability. The polar surface of TiO₂ nanotubes provides strong chemical adsorption sites for lithium polysulfides, while NiO nanoparticles enhance redox catalytic activity, and metallic Ni nanoparticles significantly improve electron transport throughout the cathode. Together, these components create a synergistic composite system that improves both the kinetics and the long-term stability of Li-S batteries. However, realizing the full potential of this composite requires further attention to interface engineering between TiO₂, NiO, and Ni phases, the development of scalable and reproducible synthesis routes, and the design of multifunctional composites that maintain performance under practical sulfur loadings. Future studies should therefore focus on these directions to bridge the gap between laboratory-scale performance and commercial viability of Li-S battery technology.

3 Chapter Three – Methodology

3.1 Preparation of TiO₂ Nanotubes decorated with Nickel oxide/Nickel nanoparticles

Titanium (IV) dioxide (99.7% Sigma-Aldrich) nanotubes were prepared by a hydrothermal method [69]. In summary, 1.5 g of anatase TiO₂ powder (99.7%, Sigma-Aldrich) was added to 100 ml of 10 M NaOH ($\geq 98\%$, Sigma-Aldrich) for 12 hours while stirring magnetically. The product formed was added to a 100 ml Teflon autoclave and heated up to 130°C in a muffle furnace for twenty-four (24) hours. The precipitate was isolated after cooling the solution to room temperature, and the precipitation process was done through centrifugation. The precipitate was repeatedly put in a 0.5 M HCl (38%, Sigma-Aldrich) solution of 500 ml and deionized water until it became neutral. Next, the precipitation was left to dry in the oven at 60 degrees centigrade overnight. It was calcinated in a muffle furnace at 600°C for 2 hours. Temperature and duration of reaction influenced the morphology of the nanotubes, wall thickness and nanotube length. In the case of surface modification, 0.11 g of nickel nitrate hexahydrate [Ni (NO₃)₂·6H₂O $\geq 97\%$ Sigma-Aldrich] was first dissolved in 1.1 ml of deionized water, after which 0.3 g of TiO₂ nanotubes prepared earlier was gradually added into a 0.5 M NaOH solution. The mixture was vigorously stirred (1000 rpm) under ambient conditions. The light-green powder obtained was immersed several times in deionized water and ethanol. The dried product was calcinated at 450 °C for 2 hours to form NiO/TiO₂ powders at the ratio 1:10[70]. For Ni/TiO₂ synthesis, the mixture of NiO/TiO₂ powders was subjected to a reduction reaction in N₂/H₂ atmosphere at 450 °C for 2 hours, resulting in the formation of TiO₂ nanotubes loaded with Ni nanoparticles in metallic form. **Fig. 1a** illustrates the steps involved in the synthesis of TiO₂ nanotubes. The resulting nanotubes were subsequently modified with NiO and Ni nanoparticles, as shown in **Fig. 1b**.

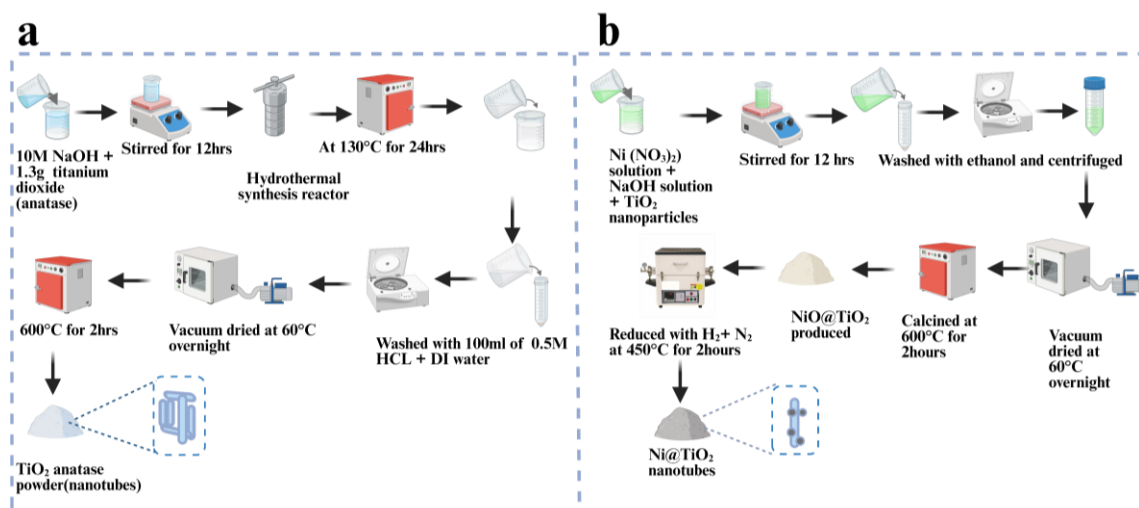


Fig. 1 Schematic illustration depicting the synthesis route of (a) TiO₂ nanotubes and (b) Decoration of NiO and Ni nanoparticles on the nanotubes.

3.2 Preparation of Cathode Materials

A slurry prepared from 30 mg of TiO₂-based samples, 0.02 g of acetylene black, 130 mg of CNTs (ISOLAB), and 20 mg of polyvinyl fluoride (Sigma-Aldrich) was mixed with a volume of 4.0 ml NMP ($\geq 99\%$, Sigma-Aldrich) in a high-speed thinky mixer and cast on carbon fibre paper (current collector) to fabricate cathodes. To ensure proper mixing, the suspension was homogenized for 300 seconds at 1200 rpm. Loading of an active material per disc was accomplished by casting about 30 μ l of the slurry on carbon nanofiber paper. Before use, the electrodes were maintained inside a vacuum oven for a period of 24 hours at a temperature of 70 °C.

3.3 Cell Assembly

Prepared TiO₂ cathodes were employed, Celgard® 2500 was chosen for the separator, and lithium metal foil as the anode in assembling CR2032 coin cells in an argon-filled MBRAUN glovebox. After application of the polysulfide solution on the dried electrode as the catholyte, the electrolyte (1M LiTFSI+2wt%LiNO₃ dissolved in a DOL/DME volume ratio of 1:1) was introduced. Extra electrolyte was injected into the anode compartment of the separator. Then, spacers and a waved spring were placed in the cell assembly before sealing the coin cell under a pressure of 100kg/cm².

3.4 Materials characterization

The structure and morphological parameters of synthesized materials were investigated by scanning electron microscopy (SEM, Zeiss Crossbeam 540, 5 kV) and transmission electron microscopy (TEM, JEOL JEM-1400PLUS, 200 kV). X-ray diffraction (XRD, Rigaku Smartlab) was used for establishing crystalline phase composition between a 2θ by utilizing Cu K α radiation ($\lambda = 1.54056 \text{ \AA}$). Thermogravimetric analysis (STA 6000, Perkin Elmer) was employed to investigate thermal behavior. Textural parameters, i.e., specific surface area and pore volume, were investigated based on nitrogen adsorption-desorption isotherms (Quantachrome Instruments) and pore size distribution by the Barrett-Joyner-Halenda (BJH) method. X-ray photoelectron spectroscopy (XPS, NEXSA, Thermo Scientific) was employed for examining the surface chemical state of elements. Elemental composition and metal loading by metal oxide composites were also investigated by inductively coupled plasma optical emission spectroscopy (ICP-OES, iCAP 6300-Thermo Scientific, England).

3.5 Electrochemical Characterization

Lithium metal was used as the counter/reference electrode, 1M Li₂S₆ solution as the catholyte, and carbon fiber paper (CFP) as the cathode current collector. Carbon-coated separators were employed in the fabrication of Li-S coin cells. 12 μl and 24 μl of 1 M Li₂S₆ solution were incorporated into each cell. Sulfur loadings, based on Li₂S₆ solutions, were 2 mg cm⁻² and 4.0 mg cm⁻² for 12 μl and 24 μl of 1 M Li₂S₆ solutions, respectively. The electrolyte: sulfur ratio was kept constant at 10:1 through the addition of 14 μl of the electrolyte to the positive electrode and 20 μL of the electrolyte to the negative electrode. Electrolyte was made up of 1M LiTFSI with 2% wt LiNO₃ in 1:1 (v/v) of DOL and DME. Charge-discharge experiments under galvanostatic conditions were carried out utilizing a Neware battery test apparatus between voltages of 1.7 to 2.8 V (relative to Li/Li⁺). CV experiments were performed on a Biologic VMP3 potentiostat/galvanostat within the voltage range, whereas EIS experiments were carried out at 5 mV amplitude from 100 kHz to 1 MHz.

3.6 Symmetric cell test

The symmetric cells were fabricated using two identical electrodes that had been synthesized, which were separated by a Celgard® 2400 membrane. For catholyte, a 0.3 M Li₂S₆ solution was used in a 1:1 ratio (v/v) of DOL/DME, and 25 μl catholyte was applied to the cathode as well as the separator. CV analysis of the electrolyte was carried out using a Biologic

VMP3 potentiostat/galvanostat with a scan rate of 20, 10, and 1 mV s⁻¹ over a potential range of -1.0 V to 1.0 V (vs. Li/Li⁺).

3.7 Nucleation test

Since the synthesized materials were loaded on the electrode surface, the CFP served as the working electrode, and metallic lithium discs (16 mm in diameter) served as the counter and reference electrodes. For the catholyte, 20 μ l of a solution of 0.5 M Li₂S₆ in tetraglyme was used, while for the anolyte, 20 μ l of 1 M lithium bis(trifluoromethanesulfonyl) imide (LiTFSI) dissolved in DOL/DME (1:1 v/v) with 2 wt% LiNO₃ was used. CR2032 coin cells were fabricated, which were then discharged galvanostatically to 2.06 V before holding them potentiostatically at 2.05 V until the current was less than 1×10^{-5} A to trigger Li₂S₆ nucleation.

4 RESULTS AND DISCUSSION

4.1 Physical Characterization of TiO₂ nanotube-based samples

In **Fig. 2a**, x-ray diffraction analysis of respective samples confirmed the anatase phase of TiO₂, as evidenced by the distinctive signals at $2\theta \approx 25.3^\circ$, 37.8° , 48.0° , 55.1° , 63.1° , 70.9° and 75.4° which is attributed to the (101), (004), (200), (211), (204), (220), and (215) crystallographic planes similar to the anatase form of TiO₂ (JCPDS 21-1271) [71]. In addition, NiO and Ni were identified by the characteristic (111) and (200) peaks near $2\theta \approx 44.5^\circ$ and 43.3° , respectively [72]. Moreover, in **Fig. 2b**, the results of thermogravimetric analysis (TGA) showed that all three samples showed a very slight initial weight loss in the range of 120 °C, which was because of the release of the physically absorbed water. Following this, there was a gradual weight loss to approximately 450 °C, which was owing to the decomposition of the residual water due to dehydroxylation. It was also noted that the maximum total weight loss occurred in the case of pure TiO₂. Nonetheless, relatively small mass losses were observed for NiO/TiO₂ and Ni/TiO₂ due to their higher thermal stability resulting from the inclusion of Nickel. In addition to this, no noticeable weight loss could be seen in any of the three samples from 450 °C to approximately 650 °C. Therefore, in this study, the most appropriate calcination temperature was determined to be 450 °C according to the TGA results. BJH theory was used to calculate pore size distribution in the sample. In addition, nitrogen adsorption-desorption isotherms were carried out on the samples (**see Fig. 2c**). They displayed a Type IV isotherm pattern in the range 0.4 -0.9 P/P₀ of relative pressure, indicating mesoporous structures with slit-like pores. The sharper uptake near 0.9 P/P₀ indicates filling of large mesopores and interparticle voids, with the blue sample showing higher adsorption capacity, suggesting larger pore volume and surface area [73]. The pore size distribution (**Fig. 2d**) shows that Ni/TiO₂ exhibits a dominant mesoporous structure with a higher pore volume than NiO/TiO₂ and the pure TiO₂, making it more suitable for applications requiring a large surface area and efficient mass transport. ICP-OES analysis (**Fig. 2e**) indicated a Ti: Ni molar ratio of approximately

10:1.

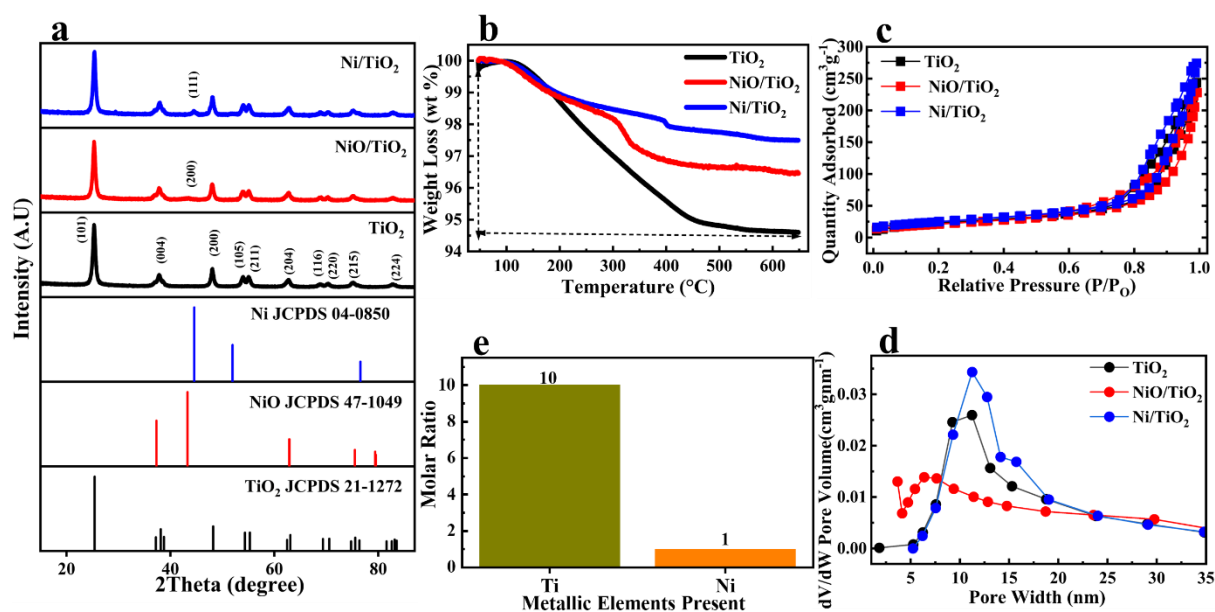


Fig. 2 Physical characterization of TiO_2 , NiO/TiO_2 , Ni/TiO_2 nanotubes: (a) XRD pattern, (b) TGA, (c) nitrogen adsorption-desorption isotherms, (d) pore size distribution and (e) ICP OES.

Fig. 3 presents a comprehensive morphological characterization of TiO_2 nanotubes and TiO_2 nanotubes modified with NiO/Ni nanoparticles using SEM and TEM imaging across multiple scales. **Fig. 3a** shows TiO_2 nanotubes with vertically aligned, smooth-walled tubular morphology, consistent with hydrothermal treatment-derived structures. These structures are known to offer high surface area and facilitate ion transport. **Fig. 3b** reveals NiO/TiO_2 with a visibly roughened surface and granular texture, resembling agglomerated NiO , which may be due to calcination. In **Fig. 3c**, TiO_2 shows a discrete nanoparticle dispersion across the TiO_2 framework with shorter lengths of the nanotube. Low-resolution TEM images of Ni/TiO_2 at 50 nm and 100 nm are shown in **Fig. 3d** and **Fig. 3e**, respectively, revealing aggregated nanostructures and confirming the decoration of Ni within the TiO_2 matrix. An additional surface morphological investigation was conducted using TEM, as seen in **Fig. 3f**. The interplanar spacing of the (101) plane of TiO_2 anatase phase was determined to be approximately 0.35 nm. For Ni nanoparticles, the interplanar spacings of the (111) and (200) planes were found to be 0.203 nm and 0.176 nm, respectively.

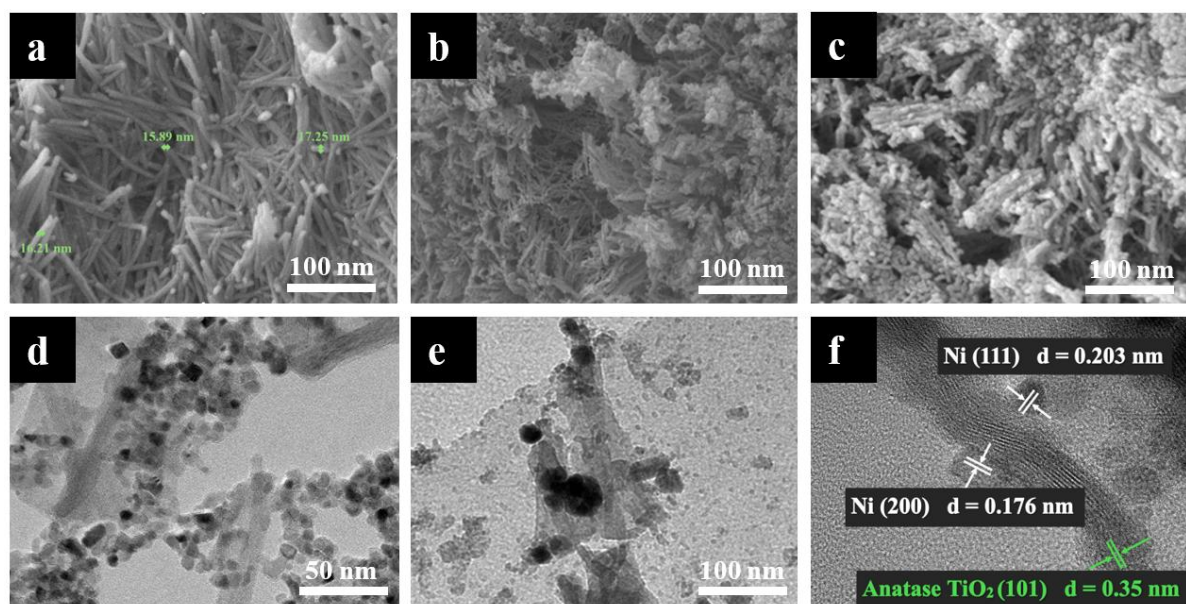


Fig. 3 SEM images of nanotubes (a) TiO_2 , (b) NiO/TiO_2 , (c) Ni/TiO_2 ; low-resolution TEM image of Ni/TiO_2 nanotubes at (d) 50 nm, (e) 100 nm and (f) HRTEM images of Ni/TiO_2 (d-spacing).

Fig. 4(a-d) shows the images of Ni/TiO_2 -CFP electrodes at magnifications ranging from low to high magnification, which display a hierarchical porous structure having interconnected domains, while EDS mapping proves the presence of Ti and Ni, respectively. This characterization process aims to verify the existence of TiO_2 nanotubes, NiO nanoparticles, and Ni nanoparticles in the cathode material. In addition, the elements have been mapped using elemental mapping to prove their even distribution. The results showed that the fragments were attached to the individual strands of carbon fibers in the cathode material.

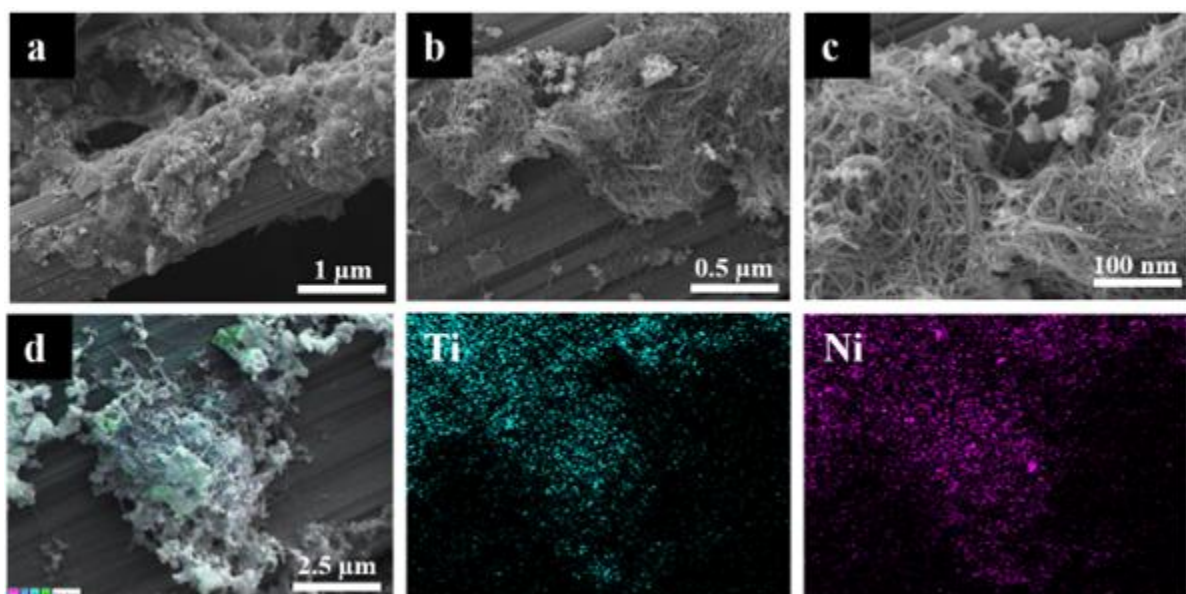


Fig. 4 SEM image of Ni/TiO₂-CFP electrodes at (a) 0.5 μ m, (b) 1 μ m, (c) 100 nm; EDS mappings of Ni/TiO₂ electrodes at (d) 100 nm.

The XPS characterization following Li₂S₆ soaking, as shown in **Fig. 5**, presents the polysulfide adsorption tendency along with chemical interactions in all the composite materials. Ti 2p spectra (**Fig. 5a**) comparing before and after Li₂S₆ soaking show that all TiO₂-containing electrodes maintain Ti 2p_{3/2} at 458.7 eV, characteristic of the Ti⁴⁺ oxidation state in TiO₂ [74], with the Ti 2p_{1/2} peak appearing at ~464.6 eV, resulting in a spin-orbit splitting of approximately 5.5 eV. After immersion in Li₂S₆, a Ti 2p shift of roughly 0.4 eV toward higher binding energy is observed, indicating a decrease in electron density around the metal centre [75]. O 1s spectra (**Fig. 5b**) after soaking reveal significant changes in oxygen chemical states: TiO₂-CFP shows increased contributions from Ti-OH (~531.5 eV) and adsorbates (~533 eV) compared to Ti-O lattice oxygen (~530 eV) [76, 77], indicating polysulfide interaction with surface hydroxyl groups. Ni 2p spectra (**Fig. 5c**) after Li₂S₆ soaking show that NiO/TiO₂-CFP maintains its Ni²⁺ character with Ni 2p_{3/2} at ~855 eV and characteristic satellite peaks at ~862 eV typical of the NiO spectrum, while Ni/TiO₂ maintains its metallic Ni signature with Ni 2p_{3/2} at ~852.7 eV [78]. The significantly higher noise level and wider peaks may suggest surface oxidation or Ni-S bonding formation that improves the polysulfide binding capability without oxidizing the entire nickel metallic core, proving that the two oxidation states of nickel play a role in the immobilization of polysulfides [79]. Moreover, a strong interaction chemistry between lithium polysulfide and Ni/Ti elements is suggested based on the formation of Ti-S bonds (164.93 eV) and Ni-S bonds (162.08 eV) [80,81]. From the above XPS analysis, the materials have been modified successfully, confirming the presence of both nickel and titanium oxidation states in the composites and their reaction with Li₂S₆, hence confirming that the polysulfides have been adsorbed, and the function of nickel and titanium in combating the shuttle effect.

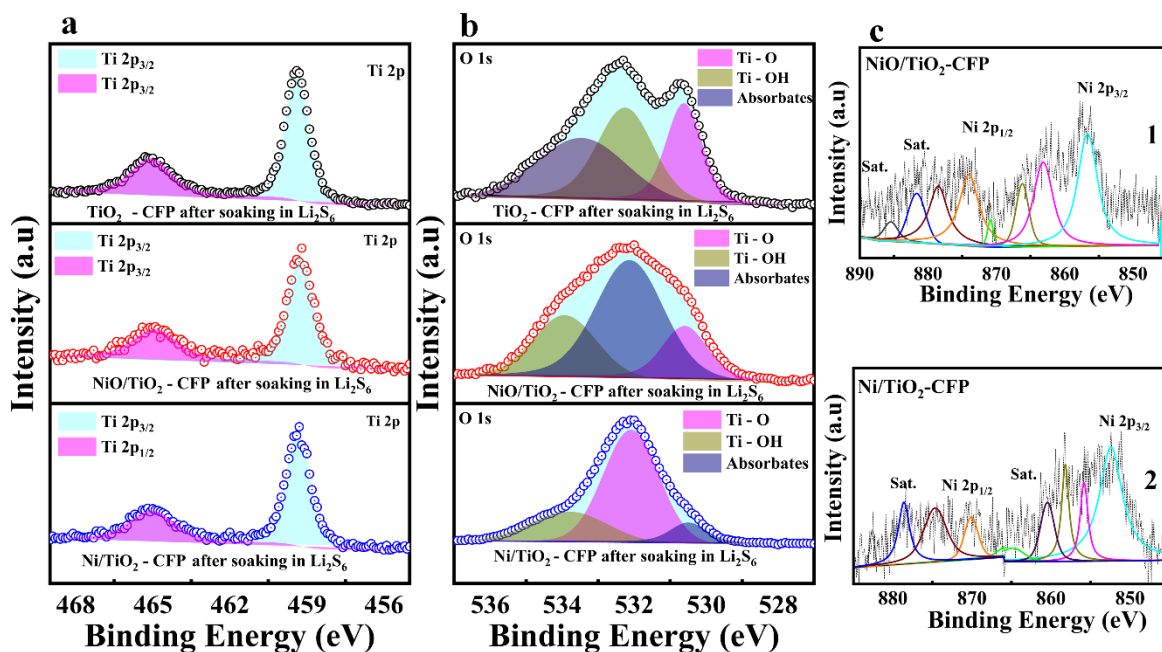


Fig. 5 XPS characterization of TiO₂, NiO/TiO₂, and Ni/TiO₂ electrodes after soaking in Li₂S₆ solution (a) Ti 2p, (b) O 1s and (c) Ni 2p (1) and Ni 2p (2).

4.2 Effect on the kinetics of redox

The effect of TiO₂ nanotubes modified with NiO and Ni nanoparticles on the redox kinetics in these cells was analysed. **Fig. 6** presents the cyclic voltammetry (CV) curves of cells with TiO₂, NiO/TiO₂, and Ni/TiO₂ electrodes at 0.1 mV s⁻¹, respectively. The CV profiles of the samples were compared to evaluate the catalytic influence of the TiO₂-based samples on the redox chemistry of sulfur species. Two pairs of reversible redox peaks were observed in the CV curve of all three TiO₂-based electrode cells. For each redox pair, the peaks were relatively sharp, suggesting faster kinetics and catalytic activity for the conversion of LiPSs [82]. The first pair of cathodic peaks was assigned to the reduction of S₈ to Li₂S₄ (peak a) and the subsequent reduction of Li₂S₄ to Li₂S (peak b). The corresponding anodic peaks were attributed to the electrochemical oxidation of Li₂S to Li₂S₄ (peak c) and the final oxidation of Li₂S₄ to S₈ (peak d), respectively [83]. The peak-to-peak separation (ΔE) between the anodic and cathodic peaks reflects the reversibility and the kinetic efficiency of the redox process. Each pair of peaks (oxidation and reduction) shows similar redox conversion pathways during cycling, as shown in **Fig. 6a-c**. However, their respective peak-to-peak separation varies due to chemical conversion rates. Therefore, peak-to-peak separation (ΔE) between pairs of peaks for coin cells with TiO₂, NiO/TiO₂ and Ni/TiO₂ electrodes are 0.24 V, 0.22 V and 0.20 V, respectively. These

results indicated that the Ni/TiO₂ electrode exhibited the lowest polarization and the fastest polysulfide conversion, whilst cells with the TiO₂ and NiO/TiO₂ electrodes showed relatively slower reaction kinetics and a slightly higher polarization.

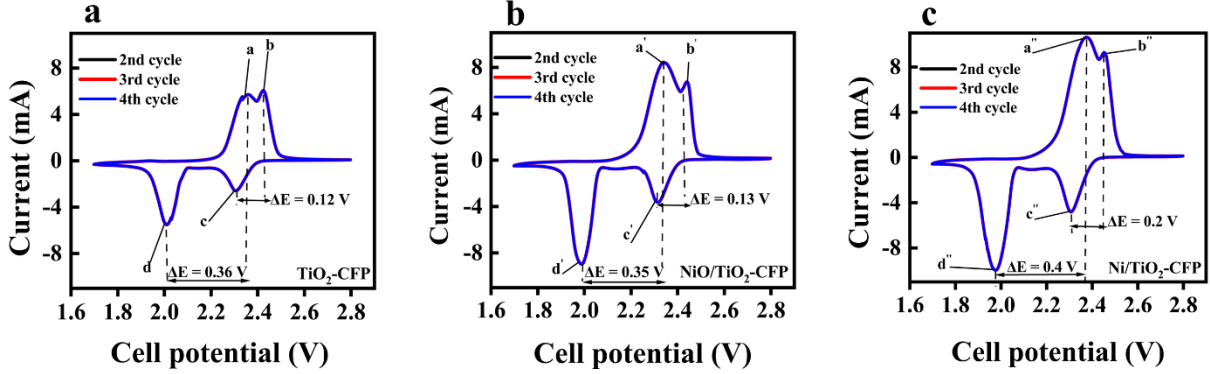


Fig. 6 Comparative cyclic voltammetry (CV) curves for all electrodes: (a) TiO₂, (b) NiO/TiO₂ and (c) Ni/TiO₂.

In addition, the CVs for all the cells with TiO₂ electrodes were measured at different scan rates between 0.1 mV/s and 0.5 mV/s, which are presented in **Fig. 7(a-c)**. The corresponding linear fittings of the peak currents versus the square root of the scan rates ($v^{1/2}$) for peak A, peak B, and peak C were obtained from the CV curves in (a-c) as presented in **Fig. 7(d-g)**. However, the purpose of the linear fittings was to determine the slopes used to calculate lithium-ion diffusion in the respective cathode materials. According to the Randles-Sevcik equation, there is a linear relationship between the redox peak current and the square root of the scan rate, which makes it possible to evaluate the diffusion of lithium ions within the electrodes [84]:

$$I_p = 2.69 \times 10^5 \times n^{3/2} \times A \times D_{Li^+}^{1/2} \times C_{Li^+} \times v^{1/2}; \quad (1.0)$$

where D_{Li^+} is the Li⁺ diffusion coefficient ($\text{cm}^2 \text{s}^{-1}$), C_{Li^+} is the concentration of lithium ions in the electrolyte (mol cm^{-3}), v is the scanning rate (V s^{-1}), I_p is the peak current (A), n is the number of electrons, and A is the electrode area (1.13097 cm^2).

While the electrode area, the number of electrons (assumed to be 2 electrons), and the concentration of lithium ions in the electrolyte remained constant, the diffusion coefficient D_{Li^+} was determined from the slope of the curve ($I_p/v^{0.5}$), which reflected the diffusion rate of lithium ions, as shown in **Table 1** [80]. It was evident that the cell with Ni/TiO₂-CFP electrode exhibited the highest lithium-ion diffusivity at peaks A and D, which mainly arose from

improved lithium polysulfide adsorption and enhanced conversion of LiPSs to Li₂S. Diffusion coefficients (D) were deduced according to the Randles-Sevcik equation based on a 12 mm electrode surface and a 1 M polysulfide solution. From Table 1, peak A, corresponding to the fastest redox process, showed that the cell with Ni/TiO₂-CFP electrode exhibited the highest value of D ($5.75 \times 10^{-6} \text{ cm}^2 \text{ s}^{-1}$), indicating rapid ion transport and effective electrochemical conversion. By contrast, peak C exhibited intermediate diffusion behaviour with a value of $2.91 \times 10^{-6} \text{ cm}^2 \text{ s}^{-1}$ for Ni/TiO₂, suggesting a moderately rapid electrochemical process. For all peaks, the cell with Ni/TiO₂ electrode exhibited the highest diffusion coefficients, followed by cells with NiO/TiO₂ and TiO₂ electrodes. Therefore, the cell with Ni/TiO₂ electrode showed better electrochemical kinetics for all redox peaks, indicating that this material is a promising electrode for improved rate performance in lithium sulfur batteries. Generally, the best diffusion enhancement for cells with Ni/TiO₂ electrode can be attributed mainly to the presence of the metallic Ni phase, which provides better electronic conductivity, promotes the transport of Li⁺ and polysulfide, and facilitates rapid interfacial charge transfer. Moreover, this phenomenon suggests faster liquid-liquid conversion of LiPSs on the electrode surface [85].

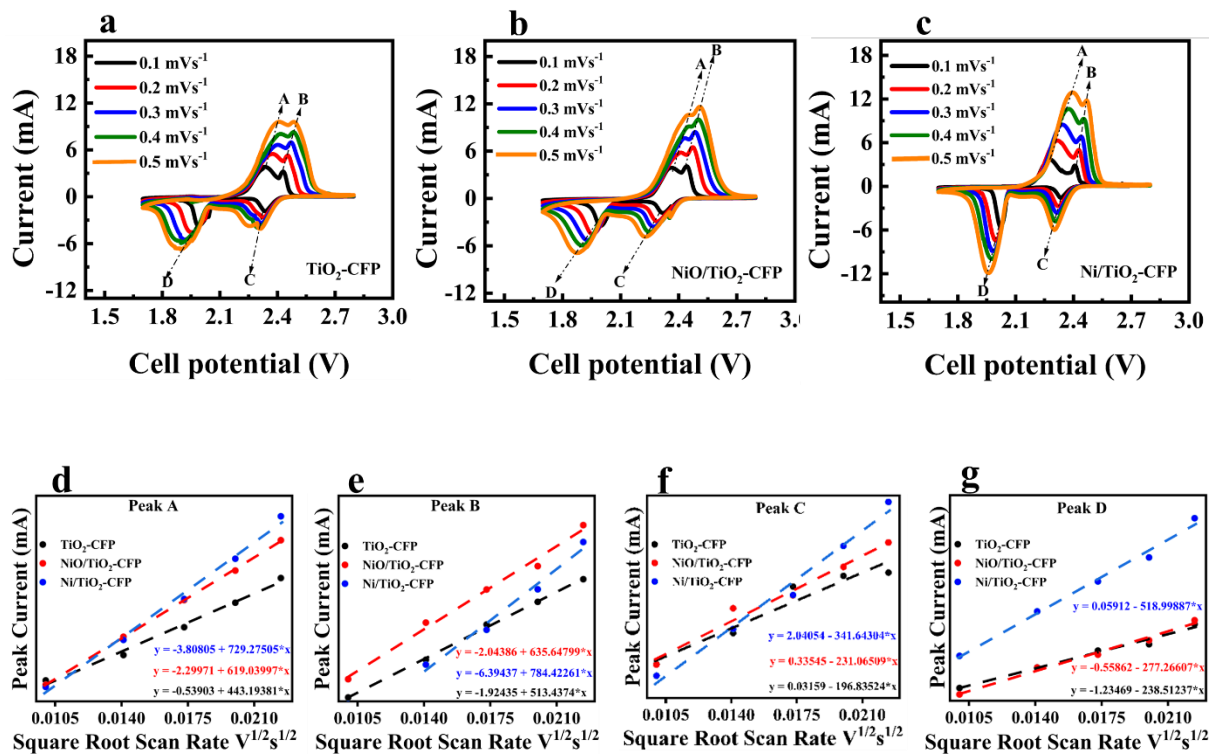


Fig. 7 CV profiles of electrodes recorded at scan rates:(a) TiO₂, (b) NiO/TiO₂ and (c) Ni/TiO₂, (d-g) The linear fittings of the peak currents versus the square root of the scan rates ($v^{1/2}$).

Table 1. Li⁺ diffusion coefficient values of TiO₂, NiO/TiO₂ and Ni/TiO₂

Electrodes	Peak A	Peak B	Peak C	Peak D
TiO ₂	2.12×10^{-6}	3.56×10^{-7}	4.19×10^{-7}	6.15×10^{-7}
NiO/TiO ₂	4.14×10^{-6}	5.46×10^{-7}	5.77×10^{-7}	8.31×10^{-7}
Ni/TiO ₂	5.75×10^{-6}	8.31×10^{-7}	1.26×10^{-6}	2.91×10^{-4}

Cyclic voltammetry recorded from symmetric cells (**Fig. 8**) shows the reduction process of lithium polysulfide. As can be seen in **Fig. 8a**, symmetric cells containing Ni/TiO₂ and NiO/TiO₂ electrodes at a 1 mVs⁻¹ scan rate had relatively higher resistance, while the TiO₂ electrode had broad loops, implying a higher resistance. On the other hand, cells having Ni/TiO₂ and NiO/TiO₂ electrodes at 10 mV s⁻¹, as depicted in **Fig. 8b**, had more symmetric peaks, good kinetics; besides, the loops were thinner and less polarized [86]. Symmetric cells having Ni/TiO₂ and NiO/TiO₂ electrodes at 20 mV s⁻¹, as depicted in **Fig. 8c**, had symmetric peaks, meaning good reversibility and low resistance based on the overlapping thin loops. Higher scan rates had better kinetic performance and lower resistances, as seen in the symmetric cell result.

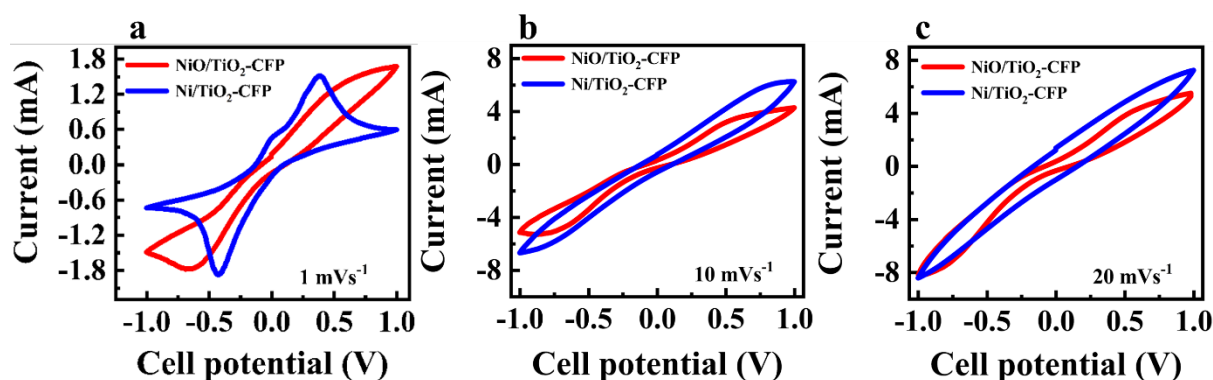


Fig. 8 CV plots of symmetric cells (NiO/TiO₂ and Ni/TiO₂) based electrodes at varying scan rates: (a) 1 mV s⁻¹, (b) 10 mV s⁻¹ and (c) 20 mV s⁻¹.

Potentiostatic charge-discharge analysis for the performance of cells with TiO₂-based electrodes was done using the Li₂S nucleation test. In this study, the current achieved by the cell having TiO₂ was highest at ~ 8370 s, as can be seen from **Fig. 9a**. While other peak response times achieved, which are ~ 7211 s and ~ 5970 s for NiO/TiO₂ and Ni/TiO₂ electrodes, respectively (**Fig. 9b & 9c**). It should be noted that Ni/TiO₂ has a better performance because it recorded the highest current after a shorter period, i.e., after ~ 5970 s. The maximum amount

of Li_2S deposition was then calculated for all cells with TiO_2 -based electrodes. From the calculations, the capacity for nucleation of Li_2S for TiO_2 , NiO/TiO_2 and Ni/TiO_2 was found to be 465 mAh g^{-1} , 600 mAh g^{-1} and 746 mAh g^{-1} , respectively.

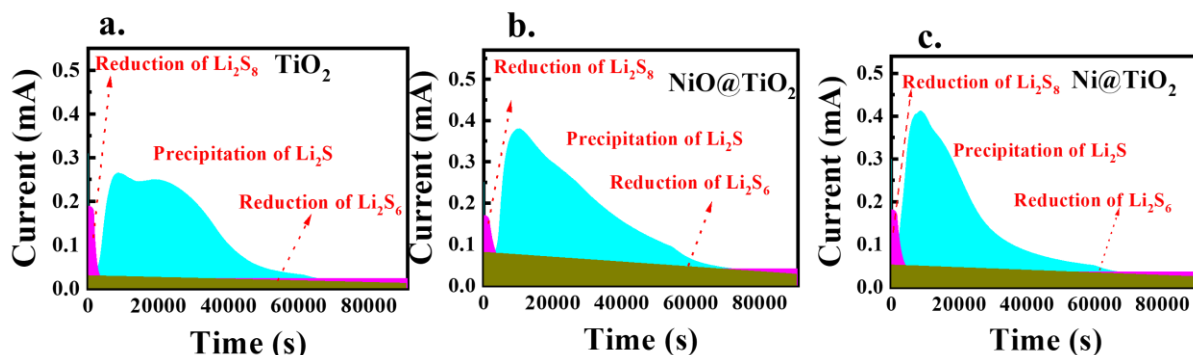


Fig. 9 Potentiostatic discharge (a) TiO_2 , (b) NiO/TiO_2 and (c) Ni/TiO_2 .

Charge transfer resistance (R_{ct}) and diffusion characteristics related to Warburg impedance (Z_w) appear to be represented by a semicircle at high frequencies and a straight line at low frequencies, according to Nyquist diagrams (Fig. 10). One can note that the charge transfer resistance (R_{ct}) values for TiO_2 , NiO/TiO_2 , and Ni/TiO_2 electrodes decrease with diminishing semicircle size, implying that kinetic impedance is low. The charge transfer resistances recorded for cells using TiO_2 -based electrodes were 46Ω , 32Ω , and 14Ω , respectively. The cell using the Ni/TiO_2 electrode exhibited the lowest initial resistance value, with $R_{ct} \approx 14 \Omega$, which implies more kinetic activity, whereas the cell with the NiO/TiO_2 ($R_{ct} \approx 32 \Omega$) and TiO_2 ($R_{ct} \approx 46 \Omega$) electrodes demonstrated increased R_{ct} values largely because of inefficient electron transfer pathways [87]. The kinetic enhancement is essential because low R_{ct} values imply quicker charge transportation, along with improved redox reactions.

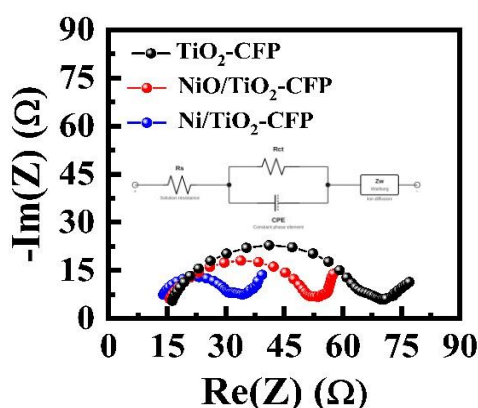


Fig. 10 Electrochemical Impedance Spectroscopy profiles for cells with TiO_2 -based electrodes.

4.3 Cycling performance of modified TiO₂-based cathodes

The charge - discharge cycling characteristics of Li-S cells with TiO₂-based cathodes (2 mg cm⁻² of sulfur), TiO₂, NiO/TiO₂, and Ni/TiO₂ cathodes, respectively, were assessed as shown in **Fig. 11a**. At 0.5 C, these cells exhibited promising initial capacities of 1053, 912, and 845 mAh g⁻¹, respectively. After 100 charge-discharge cycles, the cell's TiO₂ cathode showed the maximum capacity retention of approximately 97%. In contrast, the retention for the cells containing NiO/TiO₂ and Ni/TiO₂ cathodes decreased to approximately 70% and 74%, respectively. The average coulombic efficiencies (CE) were approximately 90%, 91%, and 87%, respectively. The cycle stability with different cathode materials was investigated at 0.2 C rates, as shown in **Fig. 11b**. Coin cells employing TiO₂, NiO/TiO₂ and Ni/TiO₂ cathodes of areal sulfur mass loadings of 2 mg cm⁻² exhibited reversible discharged capacities of 1192, 1121 and 895 mAh g⁻¹, respectively. After 100 cycles, the cell with the Ni/TiO₂ cathode retained 92% of its initial capacity. In contrast, the cells with NiO/TiO₂ and TiO₂ cathodes retained only 67% and 55%, respectively. Furthermore, the rate capability test of cells employing TiO₂, NiO/TiO₂, and Ni/TiO₂ cathodes was evaluated as illustrated in **Fig. 11c**. At current densities of 0.2, 0.5, 1, and 2 C, the cells initially generated capacities of approximately 1122, 1013.61, and 887.65 mAh g⁻¹, respectively (at 0.2 C). When the current density was reverted to 0.2 C, their respective capacities recovered to 787.58, 700 and 670 mAh g⁻¹. This indicates that while some irreversible capacity loss occurred, the TiO₂-based host significantly aids cell performance by mitigating LiPSs shuttling and accelerating the redox kinetics of sulfur and its discharge products. Moreover, the cyclic performance of all three TiO₂ based cathode materials were evaluated at a high sulfur mass loading of 4.0 mg cm⁻² and a rate of 0.2 C, as shown in **Fig. 11d**. The coin cell with Ni/TiO₂ cathode demonstrated superior performance with an initial specific capacity of approximately 1285 mAh g⁻¹ at 0.2 C with a decay rate of only 0.1% while reaching 85% of the theoretical capacity (1 C = 1675 mAh g⁻¹). After 100 cycles, the cathode maintained a capacity of approximately 1095 mAh g⁻¹, demonstrating excellent capacity retention. In contrast, the coin cell with the NiO/TiO₂ and TiO₂ cathodes exhibited comparatively lower initial specific capacities of approximately 1196.4 and 995.72 mAh g⁻¹, respectively. Coin cells with TiO₂ cathodes show relatively good capacity retention in the initial cycles, but the capacity quickly stabilizes to a low value of approximately 700 mAh g⁻¹ by 20 cycles. Coin cells with NiO/TiO₂ cathode demonstrated a rapid and significant capacity fading over the first 40 - 60 cycles. The capacity drops steadily to roughly 550 mAh g⁻¹ by the end of 100 cycles, indicating structural instability or poor suppression of the polysulfide shuttle effect. The superior specific capacity

of the coin cell with Ni/TiO₂ cathode compared to the other cathodes can be attributed to its enhanced electrical conductivity and effective electron transport pathways, which accelerate the conversion of polysulfides into Li₂S. In summary, comprehensive electrochemical analysis reveals that the coin cell with Ni/TiO₂ cathode significantly outperforms both TiO₂ and NiO/TiO₂ counterparts in terms of capacity retention, reaction rate and cycling stability, particularly under challenging conditions of high sulfur loading (4.0 mg cm⁻²).

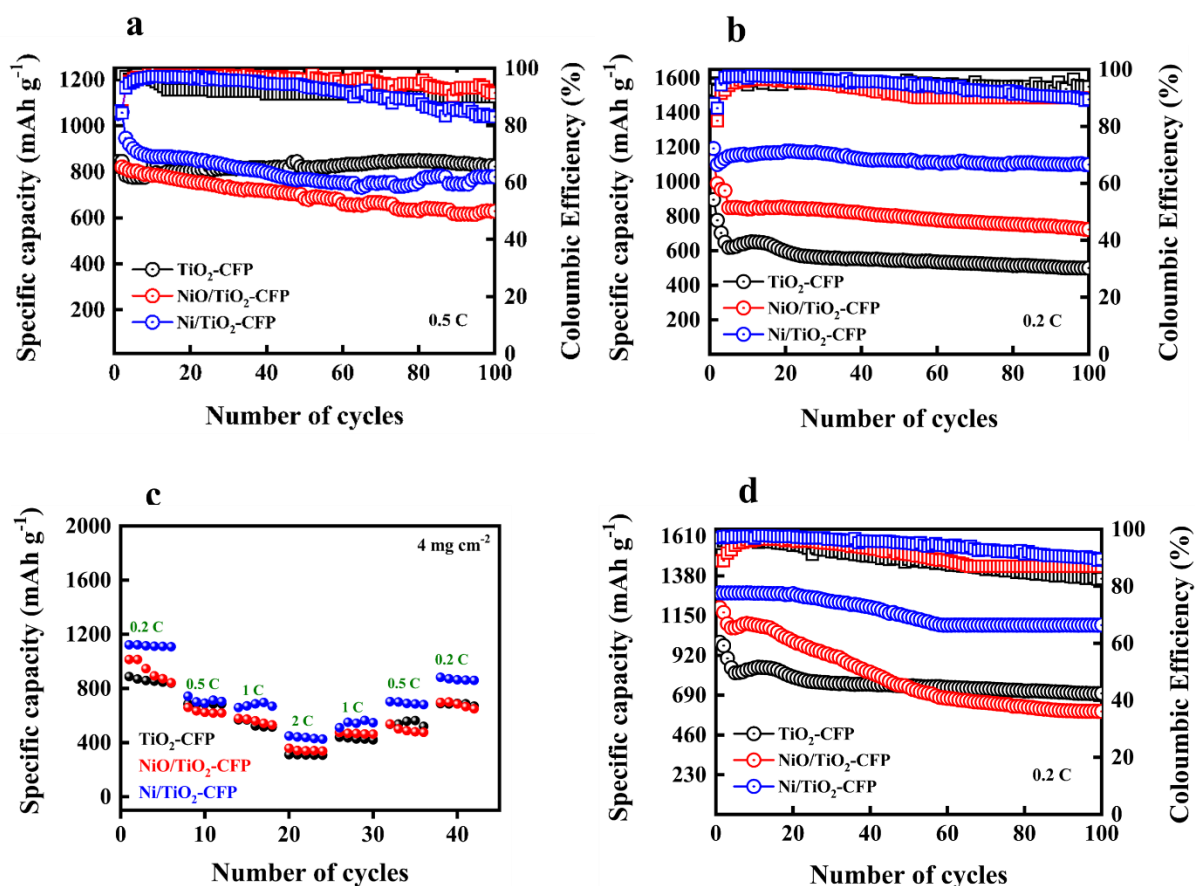


Fig. 11 (a-b) Charge-discharge cycling performance of TiO₂, NiO, and Ni/TiO₂ cathodes at 0.5 C and 0.2 C, (c) rate capability test of TiO₂, NiO/TiO₂, and Ni/TiO₂ cathodes, respectively and (d) Charge-discharge profiles of electrodes.

The galvanostatic charge-discharge profiles of Li-S cells within the voltage window of 1.6 - 2.8 V vs. Li⁺/Li at a current rate of 0.2 C were assessed as illustrated in **Fig. 12**. Every voltage graph shows a single charge plateau of about 2.4 V and two separate discharge plateaus at roughly 2.3 V and 2.1 V. These characteristics align with sulfur species' typical redox reactions. In particular, the discharge plateaus show how elemental sulfur (S₂) is gradually reduced to long-chain LiPSs, then further reduced to short-chain LiPSs (Li₂S₂ /Li₂S) [88]. The reverse

oxidation of LiPSs to elemental sulfur is reflected in the charge plateau at about 2.4 V. As indicated by **Fig. 12a**, the coin cell with the TiO_2 -based cathode had the lowest specific capacity of 1091 mAh g^{-1} . In contrast, the addition of NiO/TiO_2 and Ni/TiO_2 -based cathodes enhanced the discharge capacity and potential plateau to 1170 mAh g^{-1} and 1283 mAh g^{-1} at the 5th cycle. Moreover, Ni/TiO_2 cathode shows the lowest voltage hysteresis ($\Delta E = 0.25 \text{ V}$) among all evaluated designs compared with coin cells with NiO/TiO_2 and TiO_2 -based cathodes, indicating improved charge transfer. The galvanostatic charge-discharge profiles of the Ni/TiO_2 cathode at different cycles was also assessed as shown in **Fig. 12b**. It illustrates how Ni/TiO_2 based cathode performs when cycled under galvanostatic discharge and charge cycles, from the 2nd to the 100th cycle at 0.2 C. Initially, the voltage plates remain stable; however, from cycle number 50, there is already a noticeable gradual loss of capacity and increase in polarization gap (ΔE), termed as degradation initiation. Subsequently, with increasing cycles, capacity loss becomes prominent, and discharge voltage moves lower, indicating irreversible loss and continued degradation. The increase in polarization gap and reduction in plateau regions indicate that with extensive cycling, material modification and irreversible resistance increase to compromise its stability and performance characteristics.

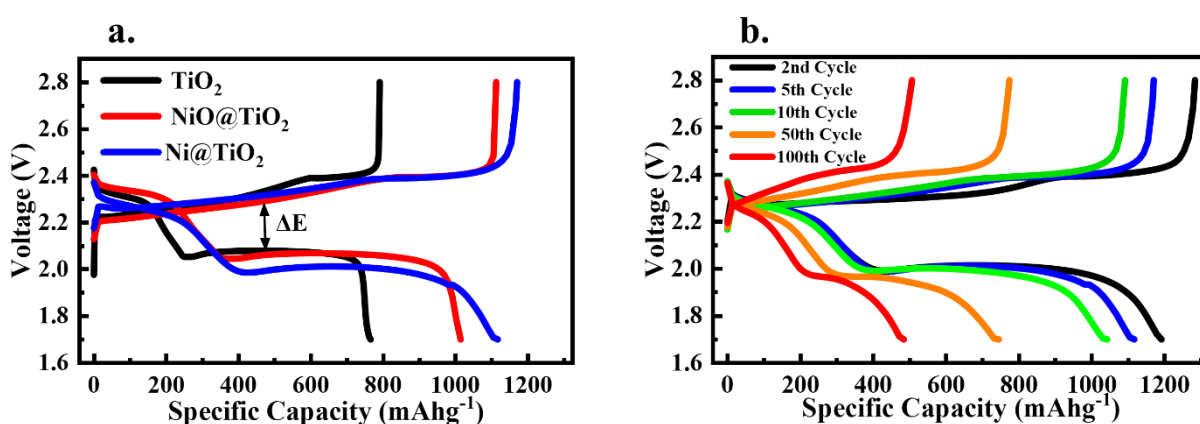


Fig. 12 (a) galvanostatic charge-discharge of TiO_2 , NiO/TiO_2 , and Ni/TiO_2 (5th cycle) and (b) galvanostatic charge-discharge profiles of cells with Ni/TiO_2 at the various cycles, respectively.

As shown in **Table 2**, a detailed comparison of TiO_2 -based nanotubes with varying average particle size and sulfur mass loading was listed with their respective electrochemical performances in terms of specific capacities and cyclic stability.

Table 2. Comparison of the electrochemical performance of TiO₂-based nanotubes

Cathode Additive	Average Particle size (nm)	Discharge Capacity (mAh g ⁻¹)	Long-term Cycling Performance	C-Rate (C)	Sulfur Loading (mg cm ⁻²)	Paper / Study
Ni/TiO ₂ Nanotubes	~18.3	1053	100	0.5	2.0	This Work
		1192	100	0.2	2.0	
		1285	100	0.2	4.0	
NiO/TiO ₂ Nanotubes		912	100	0.5	2.0	
		1121	100	0.2	2.0	
		1136	100	0.2	4.0	
TiO ₂ Nanotubes		845	100	0.5	2.0	
		895	100	0.2	2.0	
		995	100	0.2	4.0	
TiO ₂ -supported Nb Catalyst		575	350	3.0	1.0	89
		777	100	0.1	5.0	
		966	100	0.2	1.0	
TiO ₂ -Based Nanotube	10.2	721	100	0.2	1.0	
		484	350	3.0	1.0	
		632	100	0.1	5.0	
TiO ₂ -Ru@S	3-4.5	827	200	0.5	Not Reported	90
		710	700	2.0	Not Reported	
		1085	140	0.1	3.0	
TiO ₂ @S		1264	30	0.02	4.8	
		471	200	0.5	Not Reported	
S@WS ₂ - TiO ₂		560.9	1100	1	1.1	91
		455.1	100	0.2	5.878	
S@MoS ₂ - TiO ₂		634	1100	1	1.1	
		503.8	100	0.2	5.867	
S@TiO ₂		422.76	1100	1	1.1	

5 Conclusion

This study synthesized and compared three anatase TiO₂ nanotube-based cathodes, bare TiO₂-CFP, NiO/TiO₂-CFP, and Ni/TiO₂-CFP at a high sulfur loading of 4 mg cm⁻². The bare TiO₂-CFP delivered 995.72 mAh g⁻¹ at 0.2 C but was limited by poor conductivity and weak catalytic activity. NiO/TiO₂-CFP improved capacity to 1196.4 mAh g⁻¹ at 0.2 C through enhanced polysulfide chemisorption via Ni²⁺/Ni³⁺ active sites. Ni/TiO₂-CFP achieved the best performance with 1285 mAh g⁻¹ at 0.2 C, the lowest charge transfer resistance of 14 Ω, a Li₂S nucleation capacity of 745 mAh g⁻¹, 96% coulombic efficiency, and a capacity decay rate of only 0.1% per cycle, confirming metallic Ni as the most effective modifier for balancing polysulfide anchoring, catalytic conversion, and electron transport. Future work should focus on optimizing Ni loading, extending cycling beyond 100 cycles, and validating the Ni/TiO₂-CFP architecture in pouch cells at sulfur loadings above 5 mg cm⁻², and lean electrolyte conditions. This work establishes a rational design strategy for high-loading Li-S cathodes, contributing fundamental insights toward the development of commercially viable lithium-sulfur batteries with high energy density and long-term stability.

References

- [1] S. F. Ng, M. Y. L. Lau, and W. J. Ong, "Lithium–Sulfur Battery Cathode Design: Tailoring Metal-Based Nanostructures for Robust Polysulfide Adsorption and Catalytic Conversion," 2021. doi: 10.1002/adma.202008654.
- [2] S. Kaushik, T. Mehta, P. Chand, S. Sharma, and G. Kumar, "Recent advancements in cathode materials for high-performance Li-ion batteries: Progress and prospects," *J Energy Storage*, vol. 97, p. 112818, Sep. 2024, doi: 10.1016/J.EST.2024.112818.
- [3] F. Li, Q. Liu, J. Hu, Y. Feng, P. He, and J. Ma, "Recent advances in cathode materials for rechargeable lithium-sulfur batteries," 2019. doi: 10.1039/c9nr04415a.
- [4] H. J. Ahn, K. W. Kim, J. H. Ahn, and G. Cheruvally, "Secondary Batteries - Lithium Rechargeable Systems | Lithium-Sulfur," *Encyclopedia of Electrochemical Power Sources*, pp. 155–161, Jan. 2009, doi: 10.1016/B978-044452745-5.00182-9.
- [5] S. Yari, A. Conde Reis, Q. Pang, and M. Safari, "Performance benchmarking and analysis of lithium-sulfur batteries for next-generation cell design," *Nature Communications*, vol. 16, no. 1, 2025, doi: 10.1038/s41467-025-60528-4.
- [6] H. Xu *et al.*, "Review on recent advances in two-dimensional nanomaterials-based cathodes for lithium-sulfur batteries," 2023. doi: 10.1002/eom2.12286.
- [7] S. Yao *et al.*, "TiO₂ nanoparticles incorporation in carbon nanofiber as a multi-functional interlayer toward ultralong cycle-life lithium-sulfur batteries," *J Alloys Compd*, vol. 788, 2019, doi: 10.1016/j.jallcom.2019.02.236.
- [8] M. Jana *et al.*, "Rational design of two-dimensional nanomaterials for lithium-sulfur batteries," 2020. doi: 10.1039/c9ee02049g.
- [9] S. Yao *et al.*, "Synergistic effect of titanium-oxide integrated with graphitic nitride hybrid for enhanced electrochemical performance in lithium-sulfur batteries," *Int J Energy Res*, vol. 44, no. 13, 2020, doi: 10.1002/er.5671.
- [10] J. Liu *et al.*, "Efficient Regulation of Polysulfides by Anatase/Bronze TiO₂ Heterostructure/Polypyrrole Composites for High-Performance Lithium-Sulfur Batteries," *Molecules*, vol. 28, no. 11, 2023, doi: 10.3390/molecules28114286.

- [11] Z. Yang *et al.*, “Hybrid Anatase/Rutile Nanodots-Embedded Covalent Organic Frameworks with Complementary Polysulfide Adsorption for High-Performance Lithium-Sulfur Batteries,” *ACS Cent Sci*, vol. 5, no. 11, 2019, doi: 10.1021/acscentsci.9b00846.
- [12] P. Feng *et al.*, “Efficient and Homogenous Precipitation of Sulfur Within a 3D Electrospun Heterocatalytic Rutile/Anatase TiO_{2-x} Framework in Lithium–Sulfur Batteries,” *Advanced Fiber Materials*, vol. 6, no. 3, 2024, doi: 10.1007/s42765-024-00380-1.
- [13] B. Yue *et al.*, “Dual-Confinement Effect of Nanocages@Nanotubes Suppresses Polysulfide Shuttle Effect for High-Performance Lithium–Sulfur Batteries,” *Small*, vol. 20, no. 16, 2024, doi: 10.1002/sml.202308603.
- [14] M. Yu *et al.*, “Atomic layer deposited TiO₂ on a nitrogen-doped graphene/sulfur electrode for high performance lithium-sulfur batteries,” *Energy Environ Sci*, vol. 9, no. 4, 2016, doi: 10.1039/c5ee03902a.
- [15] G. S. Zakharova *et al.*, “Anatase nanotubes as an electrode material for lithium-ion batteries,” *Journal of Physical Chemistry C*, vol. 116, no. 15, 2012, doi: 10.1021/jp300955r.
- [16] J. Xu, C. Jia, B. Cao, and W. F. Zhang, “Electrochemical properties of anatase TiO₂ nanotubes as an anode material for lithium-ion batteries,” *Electrochim Acta*, vol. 52, no. 28, 2007, doi: 10.1016/j.electacta.2007.06.077.
- [17] M. M. Zhang, J. Y. Chen, H. Li, and C. R. Wang, “Recent progress in Li-ion batteries with TiO₂ nanotube anodes grown by electrochemical anodization,” 2021. doi: 10.1007/s12598-020-01499-x.
- [18] O. Fasakin *et al.*, “Preparation and physico-chemical investigation of anatase TiO₂ nanotubes for a stable anode of lithium-ion battery,” *Energy Reports*, vol. 6, 2020, doi: 10.1016/j.egy.2020.02.010.
- [19] Y. Chen *et al.*, “Nickel-decorated TiO₂ nanotube arrays as a self-supporting cathode for lithium-sulfur batteries,” *Front Mater Sci*, vol. 14, no. 3, 2020, doi: 10.1007/s11706-020-0509-5.

- [20] D. Kang, J. Li, and Y. Zhang, "Effect of Ni doping content on phase transition and electrochemical performance of TiO₂ nanofibers prepared by electrospinning applied for lithium-ion battery anodes," *Materials*, vol. 13, no. 6, 2020, doi: 10.3390/ma13061302.
- [21] S. Ma *et al.*, "Insight into Lithium–sulfur batteries performance enhancement: from metal nanoparticles to metal nanoclusters to single metal atoms," 2024. doi: 10.1007/s42864-023-00248-8.
- [22] I. Rakhimbek, N. Baikalov, A. Konarov, A. Mentbayeva, Y. Zhang, and Z. Bakenov, "Nickel and nickel oxide nanoparticle-embedded functional carbon nanofibers for lithium sulfur batteries," *Nanoscale Adv*, vol. 6, no. 2, 2023, doi: 10.1039/d3na00785e.
- [23] N. Baikalov, I. Rakhimbek, A. Konarov, A. Mentbayeva, Y. Zhang, and Z. Bakenov, "Catalytic effects of Ni nanoparticles encapsulated in few-layer N-doped graphene and supported by N-doped graphitic carbon in Li-S batteries," *RSC Adv*, vol. 13, no. 14, 2023, doi: 10.1039/d3ra00891f.
- [24] J. Li *et al.*, "Engineering Strategies for Suppressing the Shuttle Effect in Lithium–Sulfur Batteries," 2024. doi: 10.1007/s40820-023-01223-1.
- [25] A. F. Hofmann, D. N. Fronczek, and W. G. Bessler, "Mechanistic modeling of polysulfide shuttle and capacity loss in lithium-sulfur batteries," *J Power Sources*, vol. 259, 2014, doi: 10.1016/j.jpowsour.2014.02.082.
- [26] W. Ren, W. Ma, S. Zhang, and B. Tang, "Recent advances in shuttle effect inhibition for lithium sulfur batteries," 2019. doi: 10.1016/j.ensm.2019.02.022.
- [27] S. Motevalian, A. Nazir, A. Pathak, G. Jahan, D. Hamal, and B. El-Zahab, "Discretized Analysis of Polysulfide Shuttle Dynamics in Lithium-Sulfur Batteries," *J Electrochem Soc*, vol. 172, no. 4, 2025, doi: 10.1149/1945-7111/adca06.
- [28] X. Kang *et al.*, "Size Effect for Inhibiting Polysulfides Shuttle in Lithium-Sulfur Batteries," 2024. doi: 10.1002/sml.202306503.
- [29] L. Zhou *et al.*, "Sulfur Reduction Reaction in Lithium–Sulfur Batteries: Mechanisms, Catalysts, and Characterization," 2022. doi: 10.1002/aenm.202202094.
- [30] Y. Huang *et al.*, "Recent Advances and Strategies toward Polysulfides Shuttle Inhibition for High-Performance Li–S Batteries," 2022. doi: 10.1002/adv.202106004.

- [31] S. Niu *et al.*, “Modulating affinity/repulsion levels for suppressing shuttle effect of lithium polysulfides in lithium-sulfur batteries,” 2025. doi: 10.1016/j.cis.2025.103621.
- [32] Y. Zhang *et al.*, “Research on the adsorption mechanism and the effect of sulfur-inhibiting shuttle of lithium polysulfides on Mn₃O₄ for lithium-sulfur batteries,” *Comput Mater Sci*, vol. 246, 2025, doi: 10.1016/j.commatsci.2024.113376.
- [33] Y. Kong *et al.*, “Co/Mon Invigorated Bilateral Kinetics Modulation for Advanced Lithium–Sulfur Batteries,” *Advanced Materials*, vol. 36, no. 13, 2024, doi: 10.1002/adma.202310143.
- [34] Z. X. Chen *et al.*, “Cathode Kinetics Evaluation in Lean-Electrolyte Lithium-Sulfur Batteries,” *J Am Chem Soc*, vol. 145, no. 30, 2023, doi: 10.1021/jacs.3c02786.
- [35] X. Y. Li *et al.*, “Kinetic Evaluation on Lithium Polysulfide in Weakly Solvating Electrolyte toward Practical Lithium-Sulfur Batteries,” *J Am Chem Soc*, vol. 146, no. 21, 2024, doi: 10.1021/jacs.4c02603.
- [36] Z. Wang *et al.*, “Steric Hindrance-Induced Amorphous Lithium Sulfide Deposition Accelerates Sulfur Redox Kinetics in Lithium–Sulfur Batteries,” *Advanced Materials*, vol. 37, no. 29, 2025, doi: 10.1002/adma.202504715.
- [37] W. Xiao, K. Yoo, J. H. Kim, and H. Xu, “Decoupling Redox Kinetics with Complementary d-Band Catalysis for High-Performance Lithium-Sulfur Batteries,” *ACS Nano*, vol. 19, no. 25, 2025, doi: 10.1021/acsnano.5c05449.
- [38] P. Wang, B. Xi, M. Huang, W. Chen, J. Feng, and S. Xiong, “Emerging Catalysts to Promote Kinetics of Lithium–Sulfur Batteries,” 2021. doi: 10.1002/aenm.202002893.
- [39] P. Zhang *et al.*, “Vanadium-Doped Molybdenum Diselenide Accelerates Sulfur Redox Kinetics in Lithium–Sulfur Batteries,” *Small Methods*, vol. 9, no. 8, 2025, doi: 10.1002/smtd.202500255.
- [40] G. Korotcenkov, “Current trends in nanomaterials for metal oxide-based conductometric gas sensors: Advantages and limitations. part 1: 1D and 2D nanostructures,” 2020. doi: 10.3390/nano10071392.
- [41] R. S. Devan, R. A. Patil, J. H. Lin, and Y. R. Ma, “One-dimensional metal-oxide nanostructures: Recent developments in synthesis, characterization, and applications,” *Adv Funct Mater*, vol. 22, no. 16, 2012, doi: 10.1002/adfm.201201008.

- [42] C. Bandas, C. Orha, M. Nicolaescu, M. I. Morariu, and C. Lăzău, “2D and 3D Nanostructured Metal Oxide Composites as Promising Materials for Electrochemical Energy Storage Techniques: Synthesis Methods and Properties,” 2024. doi: 10.3390/ijms252312521.
- [43] P. Kumbhakar *et al.*, “Emerging 2D metal oxides and their applications,” 2021. doi: 10.1016/j.mattod.2020.11.023.
- [44] H. Xie *et al.*, “Recent advances in the fabrication of 2D metal oxides,” 2022. doi: 10.1016/j.isci.2021.103598.
- [45] R. K. Joshi and J. J. Schneider, “Assembly of one dimensional inorganic nanostructures into functional 2D and 3D architectures. Synthesis, arrangement and functionality,” *Chem Soc Rev*, vol. 41, no. 15, 2012, doi: 10.1039/c2cs35089k.
- [46] M. S. Chavali and M. P. Nikolova, “Metal oxide nanoparticles and their applications in nanotechnology,” 2019. doi: 10.1007/s42452-019-0592-3.
- [47] H. Park *et al.*, “Heterostructured nickel–cobalt metal alloy and metal oxide nanoparticles as a polysulfide mediator for stable lithium–sulfur full batteries with lean electrolyte,” *Carbon Energy*, vol. 6, no. 7, 2024, doi: 10.1002/cey2.472.
- [48] Y. L. Luo *et al.*, “Carbon Nanotubes-Doped Metal Oxides and Metal Sulfides Heterostructure Achieves 3D Morphology Deposition of Li₂S and Stable Long-Cycle Lithium–Sulfur Batteries,” *Inorganics (Basel)*, vol. 13, no. 6, 2025, doi: 10.3390/inorganics13060181.
- [49] J. Y. Cheong, S. H. Cho, J. Lee, J. W. Jung, C. Kim, and I. D. Kim, “Multifunctional 1D Nanostructures toward Future Batteries: A Comprehensive Review,” 2022. doi: 10.1002/adfm.202208374.
- [50] X. Tao *et al.*, “Balancing surface adsorption and diffusion of lithium-polysulfides on nonconductive oxides for lithium-sulfur battery design,” *Nat Commun*, vol. 7, 2016, doi: 10.1038/ncomms11203.
- [51] S. I. Sadia *et al.*, “Crystallographic biography on nanocrystalline phase of polymorphs titanium dioxide (TiO₂): A perspective static review,” 2024. doi: 10.1016/j.sajce.2024.07.005.

- [52] D. R. Eddy *et al.*, “Heterophase Polymorph of TiO₂ (Anatase, Rutile, Brookite, TiO₂ (B)) for Efficient Photocatalyst: Fabrication and Activity,” 2023. doi: 10.3390/nano13040704.
- [53] A. Solomon, “Synthesis, Modification, Applications and Challenges of Titanium Dioxide Nanoparticles,” *Research Journal of Nanoscience and Engineering*, vol. 3, no. 4, 2019, doi: 10.22259/2637-5591.0304003.
- [54] O. Durante *et al.*, “Emergence and evolution of crystallization in tio₂ thin films: A structural and morphological study,” *Nanomaterials*, vol. 11, no. 6, 2021, doi: 10.3390/nano11061409.
- [55] N. Liu, X. Chen, J. Zhang, and J. W. Schwank, “A review on TiO₂-based nanotubes synthesized via hydrothermal method: Formation mechanism, structure modification, and photocatalytic applications,” *Catal Today*, vol. 225, 2014, doi: 10.1016/j.cattod.2013.10.090.
- [56] W. Luo and A. Taleb, “Large-scale synthesis route of TiO₂ nanomaterials with controlled morphologies using hydrothermal method and TiO₂ aggregates as precursor,” *Nanomaterials*, vol. 11, no. 2, 2021, doi: 10.3390/nano11020365.
- [57] S. Sassi, A. Bouich, B. Bessais, L. Khezami, B. M. Soucase, and A. Hajjaji, “Comparative Analysis of Anodized TiO₂ Nanotubes and Hydrothermally Synthesized TiO₂ Nanotubes: Morphological, Structural, and Photoelectrochemical Properties,” *Materials*, vol. 17, no. 21, 2024, doi: 10.3390/ma17215182.
- [58] B. Çalışkan and E. Şayan, “Review on TiO₂ nanotubes in dye-sensitized solar cells: electrochemical anodization and hydrothermal method,” 2025. doi: 10.1007/s10008-024-06168-y.
- [59] B. Uzunbayir, U. Kartal, E. C. Doluel, M. Yurddaskal, and M. Erol, “Development of α -Fe₂O₃/TiO₂ 3D hierarchical nanostructured photocatalysts through electrochemical anodization and sol–gel methods,” *J Solgel Sci Technol*, vol. 96, no. 2, 2020, doi: 10.1007/s10971-020-05405-w.
- [60] Y. L. Pang, S. Lim, H. C. Ong, and W. T. Chong, “A critical review on the recent progress of synthesizing techniques and fabrication of TiO₂-based nanotubes photocatalysts,” 2014. doi: 10.1016/j.apcata.2014.05.007.

- [61] J. Chen *et al.*, “Oxygen vacancies and phase tuning of self-supported black TiO₂-X nanotube arrays for enhanced sodium storage,” *Chemical Engineering Journal*, vol.400, 2020, doi: 10.1016/j.cej.2020.125784.
- [62] A. A. Abdelhafiz *et al.*, “Defect engineering in 1D Ti-W oxide nanotube arrays and their correlated photoelectrochemical performance,” *Physical Chemistry Chemical Physics*, vol. 20, no. 15, 2018, doi: 10.1039/c8cp01413b.
- [63] S. J. Patil, “Synthesis Approaches and Applications of Nickel Oxide Nanoparticles,” *International Journal of Innovative Research in Engineering & Multidisciplinary Physical Sciences*, vol. 11, no. 4, 2023.
- [64] G. T. Anand, R. Nithiyavathi, R. Ramesh, S. John Sundaram, and K. Kaviyarasu, “Structural and optical properties of nickel oxide nanoparticles: Investigation of antimicrobial applications,” *Surfaces and Interfaces*, vol. 18, 2020, doi: 10.1016/j.surfin.2020.100460.
- [65] N. D. Jaji, H. L. Lee, M. H. Hussin, H. M. Aki1, M. R. Zakaria, and M. B. H. Othman, “Advanced nickel nanoparticles technology: From synthesis to applications,” 2020. doi: 10.1515/ntrev-2020-0109.
- [66] Y. Yang *et al.*, “Gamma-radiation induced synthesis of freestanding nickel nanoparticles,” *Dalton Transactions*, vol. 50, no. 1, 2021, doi: 10.1039/d0dt03223a.
- [67] X. Wang *et al.*, “Enhanced photoelectrochemical performance of NiO-doped TiO₂ nanotubes prepared by an impregnation—calcination method,” *J Chem Res*, vol. 45, no. 11-12, 2021, doi: 10.1177/174751982111056285.
- [68] M. Zayed, S. Samy, M. Shaban, A. S. Altowyan, H. Hamdy, and A. M. Ahmed, “Fabrication of TiO₂/NiO p-n Nanocomposite for Enhancement Dye Photodegradation under Solar Radiation,” *Nanomaterials*, vol. 12, no. 6, 2022, doi: 10.3390/nano12060989.
- [69] T. Kasuga, M. Hiramatsu, A. Hoson, T. Sekino, and K. Niihara, “Formation of Titanium Oxide Nanotube,” *Langmuir*, vol. 14, no. 12, pp. 3160–3163, Jun. 1998, doi: 10.1021/la9713816.
- [70] Y. Bahari Molla Mahaleh, S. K. Sadrnezhaad, and D. Hosseini, “NiO Nanoparticles Synthesis by Chemical Precipitation and Effect of Applied Surfactant on Distribution of

- Particle Size,” *J. Nanomater.*, vol. 2008, no. 1, p. 470595, Jan. 2008, doi: 10.1155/2008/470595.
- [71] Y. Chen *et al.*, “Nickel-decorated TiO₂ nanotube arrays as a self-supporting cathode for lithium-sulfur batteries,” *Front. Mater. Sci.*, vol. 14, no. 3, pp. 266–274, Sep. 2020, doi: 10.1007/s11706-020-0509-5.
- [72] H. Wang, X. Kou, L. Zhang, and J. Li, “Size-controlled synthesis, microstructure and magnetic properties of Ni nanoparticles,” *Mater. Res. Bull.*, vol. 43, no. 12, pp. 3529–3536, Dec. 2008, doi: 10.1016/j.materresbull.2008.01.012.
- [73] J. Lynch, C. Giannini, J. K. Cooper, A. Loiudice, I. D. Sharp, and R. Buonsanti, “Substitutional or Interstitial Site-Selective Nitrogen Doping in TiO₂ Nanostructures,” *J. Phys. Chem. C*, vol. 119, no. 13, pp. 7443–7452, Apr. 2015, doi: 10.1021/jp512775s.
- [74] C. Li *et al.*, “Conductive and Polar Titanium Boride as a Sulfur Host for Advanced Lithium–Sulfur Batteries,” *Chem. Mater.*, vol. 30, no. 20, pp. 6969–6977, Oct. 2018, doi: 10.1021/acs.chemmater.8b01352.
- [75] H.-B. Kim and D.-J. Jang, “Morphological variation of anatase TiO₂ crystals via formation of titanium glycerolate precursors under microwave irradiation,” *CrystEngComm*, vol. 17, no. 17, pp. 3325–3332, 2015, doi: 10.1039/C5CE00257E.
- [76] J. Ni, S. Fu, C. Wu, J. Maier, Y. Yu, and L. Li, “Self-Supported Nanotube Arrays of Sulfur-Doped TiO₂ Enabling Ultrastable and Robust Sodium Storage,” *Adv. Mater.*, vol. 28, no. 11, pp. 2259–2265, Mar. 2016, doi: 10.1002/adma.201504412.
- [77] A. P. Grosvenor, M. C. Biesinger, R. St. C. Smart, and N. S. McIntyre, “New interpretations of XPS spectra of nickel metal and oxides,” *Surf. Sci.*, vol. 600, no. 9, pp. 1771–1779, May 2006, doi: 10.1016/j.susc.2006.01.041.
- [78] M. Chen *et al.*, “Kinetically elevated redox conversion of polysulfides of lithium-sulfur battery using a separator modified with transition metals coordinated g-C₃N₄ with carbon-conjugated.
- [79] M. Chen *et al.*, “Kinetically elevated redox conversion of polysulfides of lithium-sulfur battery using a separator modified with transition metals coordinated g-C₃N₄ with carbon-conjugated,” *Chem. Eng. J.*, vol. 385, p. 123905, Apr. 2020, doi: 10.1016/j.cej.2019.123905.

- [80] K. Xiao *et al.*, “N-doped carbon sheets arrays embedded with CoP nanoparticles as high-performance cathode for Li-S batteries via triple synergistic effects,” *J. Power Sources*, vol. 455, p. 227959, Apr. 2020, doi: 10.1016/j.jpowsour.2020.227959.
- [81] S. Zhang, “Liquid electrolyte lithium/sulfur battery: Fundamental chemistry, problems, and solutions,” *J. Power Sources*, vol. 231, pp. 153–162, Jun. 2013, doi: 10.1016/j.jpowsour.2012.12.102.
- [82] J. Wang *et al.*, “Single-atom catalyst boosts electrochemical conversion reactions in batteries,” *Energy Storage Mater.*, vol. 18, pp. 246–252, Mar. 2019, doi: 10.1016/j.ensm.2018.09.006.
- [83] S. Azam, Z. Wei, and R. Wang, “Adsorption-catalysis design with cerium oxide nanorods supported nickel-cobalt-oxide with multifunctional reaction interfaces for anchoring polysulfides and accelerating redox reactions in lithium sulfur battery,” *J. Colloid Interface Sci.*, vol. 635, pp. 466–480, Apr. 2023, doi: 10.1016/j.jcis.2022.12.130.
- [84] D. Liu, H. Li, K. Li, and M. Zhen, “Adsorption, diffusion and electrocatalytic triple effect from ultrathin-walled TiO₂(B) nanotubes for lithium–sulfur batteries,” *J. Taiwan Inst. Chem. Eng.*, vol. 132, p. 104164, Mar. 2022, doi: 10.1016/j.jtice.2021.104164.
- [85] Azam, S.; Wei, Z.; Wang, R. Adsorption-Catalysis Design with Cerium Oxide Nanorods Supported Nickel-Cobalt-Oxide with Multifunctional Reaction Interfaces for Anchoring Polysulfides and Accelerating Redox Reactions in Lithium Sulfur Battery. *J. Colloid Interface Sci.* **2023**, 635, 466–480. <https://doi.org/10.1016/j.jcis.2022.12.130>.
- [86] Pu, J.; Shen, Z.; Zheng, J.; Wu, W.; Zhu, C.; Zhou, Q.; Zhang, H.; Pan, F. Multifunctional Co₃S₄@sulfur Nanotubes for Enhanced Lithium-Sulfur Battery Performance. *Nano Energy* **2017**, 37, 7–14. <https://doi.org/10.1016/j.nanoen.2017.05.009>.
- [87] A. Ch. Lazanas and M. I. Prodromidis, “Electrochemical Impedance Spectroscopy—A Tutorial,” *ACS Meas. Sci. Au*, vol. 3, no. 3, pp. 162–193, Jun. 2023, doi: 10.1021/acsmeasuresciau.2c00070.
- [88] M. A. Al-Tahan, Y. Dong, R. Zhang, Y. Zhang, and J. Zhang, “Understanding the high-performance Fe(OH)₃@GO nanoarchitecture as effective sulfur hosts for the high capacity of lithium-sulfur batteries,” *Appl. Surf. Sci.*, vol. 538, p. 148032, Feb. 2021, doi: 10.1016/j.apsusc.2020.148032.

- [89] Barlow, Z.; Wei, Z.; Wang, R. Boosting Lithium Polysulfide Conversion via TiO₂-Supported Niobium Catalyst for Lithium Sulfur Battery. *Mater. Chem. Phys.* **2024**, *314*, 128830. <https://doi.org/10.1016/j.matchemphys.2023.128830>.
- [90] Pu, J.; Zhu, G.; Chang, S.; Zhu, X.; Wang, Z.; Xue, P. Interfacial Engineering of Ru Nanocluster-Modified TiO₂ Nanotube-Assisted Regulation of Lithium Polysulfide Reactions. *Inorg. Chem.* **2023**, *62* (44), 18307–18314. <https://doi.org/10.1021/acs.inorgchem.3c03163>.
- [91] Meng, X.; Chen, Z.; Hong, S.; Jin, L.; Liu, H.; He, C.; Che, Y.; Zhang, Z.; Yu, J.; Yang, Z.; Cai, J. TiO₂ Nanotubes Loaded WS₂/MoS₂ to Construct Heterostructures to Accelerate the Conversion of Polysulfide in Lithium–Sulfur Batteries. *Mater. Today Chem.* **2024**, *42*, 102351. <https://doi.org/10.1016/j.mtchem.2024.102351>.